Methodology for tidal turbine representation in ocean circulation model

Roc, T

Methodology for Tidal Turbine Representation in Ocean Circulation Model

Thomas Roc[1], Daniel C. Conley[1] and Deborah Greaves[1]

1 University of Plymouth,
School of Marine Science and Engineering,
Portland Square A410, Drake Circus, Plymouth PL48AA, Devon, UK
E-mail: www.plymouth.ac.uk

Abstract

The present method proposes the use and adaptation of ocean circulation models as an assessment tool framework for tidal current turbine (TCT) array-layout optimization. By adapting both momentum and turbulence transport equations of an existing model, the present TCT representation method is proposed to extend the actuator disc concept to 3-D large scale ocean circulation models. Through the reproduction of experimental flume tests and grid dependency tests, this method has shown its numerical coherence as well as its ability to simulate accurately both momentum and turbulent turbine-induced perturbations in both near and far wakes in a relatively short period of computation time. Consequently the present TCT representation method is a very promising basis for the development of a TCT array layout optimization tool.

Keywords

Optimization, tidal, turbine, layout, wake, turbulence

1. Introduction

Channel constrictions in which strong currents are mainly driven by tidal processes represent sites with high potential for harvesting renewable and predictable energy. Tidal Current Turbines (TCTs) deployed in arrays appear to be the most promising solution to efficiently capture this carbon neutral energy resource. However to ensure the sustainable character of such projects, the balance between power extraction maximization and impact minimization must be found so that device layout optimization take into account environmental considerations. This is particularly appropriate since both resource and impact assessments go intrinsically hand in hand. It has been demonstrated in numerous articles (Pham & Martin, 2009; Salter, 2009; Bryden & Couch, 2004; Bryden & Couch, 2007; Garrett & Cummins, 2005; Blunden & Bahaj, 2007) that assessment methods of tidal energy harvesting based solely on undistributed flow considerations, without integrating any feedbacks due to TCT hydrodynamic influences, misrepresent the real potential of exploitable sites and the potential hydrodynamic impacts of TCT array layouts. In fact the potential for energy extraction can be increased by taking into account and making the use of turbine induced impacts (Salter, 2009; Couch & Bryden, 2006; Bryden & Melville, 2004). Deployment optimization includes wake interactions with turbines (Bai, et al., 2009). Indeed, wake shapes, extensions and decays are sensitive to internal and surface waves (Maganga, et al., 2009; Salter, 2009), flow alignment (O'Doherty, et al., 2009) and turbulence intensity (Harrison, et al., 2009). Reciprocally, turbine yields

1

are affected by upstream-turbine wakes through the characteristic velocity deficits and increase in turbulence (Gretton, et al., 2009). Thus a relevant device layout optimization must account for all those parameters and at the same time enable the identification of potentially harmful hydrodynamic effects such as those on sediment transport processes induced by the presence of devices in the channel flow. In summary, one can say that in order to ensure the sustainable and renewable character of a large-scale TCT farm, a mutual resource-impact regional assessment must be performed during the pre-deployment phase. The scope of such an investigation requires examination of 3-D multi-scale phenomenon, from sub-grid scale turbulences to channel velocity and water-level perturbations.

The ultimate aim of this research is to create an appropriate modeling system for such optimization investigations. As analytical approaches cannot be utilized for the level of complexity inherent in realistic cases, this manuscript focuses on representing tidal current turbines in a numerical model which can be applied to spatial scales sufficient to represent the area of most significant impact. It has been decided to accomplish this through the adaptation of an existing ocean circulation model by including a TCT representation. After examining a wide range of models for their key numerical features and practical implementation considerations, ROMS (Regional Ocean Modeling System (Website, n.d.)) stood out as the best suited base model upon which to build such a tool. The main innovations of the TCT representation presented here lie in the fact that it treats each individual device as a mid-water column perturbation, accounting for both momentum and turbulent hydrodynamic-effects, itself implemented in a regional ocean circulation modeling framework. This has required implementation of techniques borrowed from high resolution Computational Fluid Dynamics (CFD) as well as coarse resolution ocean-circulation models and developed for various research fields such as wind energy or forest canopy research.

After a background presentation of the theoretical basis of the TCT representation method, the manuscript describes the base model ROMS, the framework of the numerical tool, as well as the model modifications and the implementation scheme used to inject this method into ROMS. Thereafter the validation exercise and benchmarking methodology are introduced and followed by series of standard numerical spatial grid dependency tests. The method is then applied to a TCT case study and the results compared with published experimental data.

2. Physics of Turbine forcing

Before going any further, let's define few notations used throughout the present document. Let be q any scalar quantity or vector:

$$\begin{cases} \overline{q} = Q = temporal\ average\ q \\ \langle q \rangle_i = spatial\ average\ of\ q\ along\ the\ i^{th}\ direction \\ q = Q + q' = Reynolds\ decomposition\ of\ q \end{cases}$$

The triplet $i, j, k = \{x, y, z\}$ is defined in a Cartesian basis. Let be $\vec{v}$ the velocity vector in the Cartesian basis defined by the set of unitary vectors $(\overrightarrow{e_x}, \overrightarrow{e_y}, \overrightarrow{e_z})$:

$$\vec{v} = \begin{vmatrix} u.\overrightarrow{e_x} \\ v.\overrightarrow{e_y} \\ w.\overrightarrow{e_z} \end{vmatrix} \begin{matrix} \overrightarrow{v_h} \\ \overrightarrow{v_v} \end{matrix} = \begin{vmatrix} (U + u').\overrightarrow{e_x} \\ (V + v').\overrightarrow{e_y} \\ (W + w').\overrightarrow{e_z} \end{vmatrix} = \vec{V} + \overrightarrow{v'}$$

2.1. Actuator Disc Theory – Introduction and Limitations

The presence of a TCT in a flow is intended to harness some of its energy. The energy extracted from the flow is converted into useable power from the torque applied on the rotor by the fluid flow and the torque itself is induced by the design of the blades. In the opposite reaction, the fluid acquires a swirl-like rotational motion downstream of the turbine. This area of reduced axial momentum and increased angular momentum extending several rotor diameter lengths is called the wake. Commonly the wake structure is divided in two parts: the near and the far wake (Pham & Martin, 2009). The near wake is characterized by flow which exhibits high turbulence levels mainly generated by the axial velocity shear, blade related vortices and wake rotation (Réthoré, et al., 2009; Kasmi & Masson, 2008). Assuming a regional scale focus, the details of the induced swirl effects in the near wake region are not of great relevance to TCT modeling (Salter, 2009; Bryden & Couch, 2007). This assumption is inherent in the physical scale modeling practice in which turbines are represented by non-rotating porous discs (Bryden & Couch, 2004; Bryden & Couch, 2007; Garrett & Cummins, 2005). This experimental approach is often compared to the actuator disc concept (Myers & Bahaj, 2010), itself commonly used in numerical simulation and analytical models (Harrison, et al., 2009).

According to the actuator disc concept (Figure 1), extracting energy from a fluid flow requires a reduction in the momentum of the fluid passing through the area swept by the turbine blades, often referred to as an actuator disc. Simultaneously, fluid passing through the rotor experiences a discontinuity in static pressure p along the rotor-center line, namely at the rotor location $p_d^+ \neq p_d^-$ (Burton, et al., 2008).
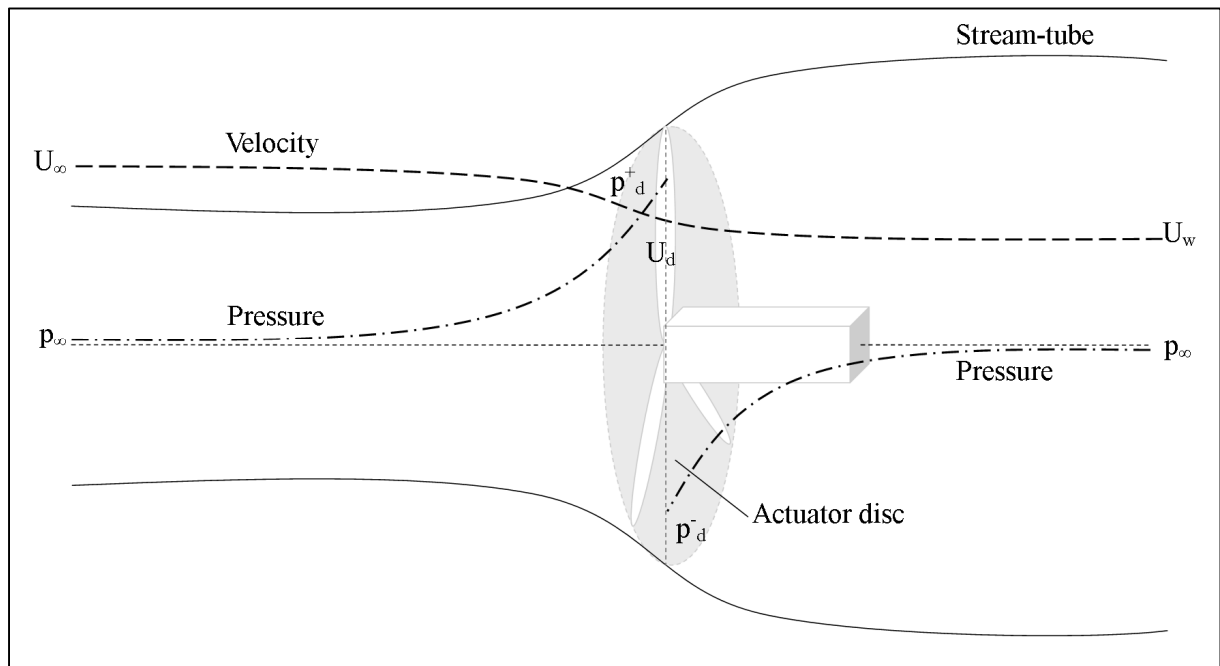

Figure 1: Actuator disc theory - Conceptual diagram. The diagram displays the actuator disc (grey surface), the turbine hub (white box and the white blades), stream-tube (delineated by solid lines), approximated velocity (heavy dashed lines) and pressure magnitudes (heavy dotted-dashed lines). The fluid flows from left to right. After Burton *et al.* (2008).

These particular dynamics are commonly formalized through Momentum Theory (Burton, et al., 2008) in which the mass flow rate is considered the same everywhere along the stream-tube (Figure 1). Accordingly, the pressure drop induced by the presence of a TCT can be expressed as follows:

$$(p_d^+ - p_d^-) = (U_\infty - U_w)\rho U_\infty(1 - a) \tag{1}$$

where a is the induction factor ($= \frac{U_\infty - U_d}{U_\infty}$), $p_d^{+,-}$ the pressure before and behind the disc, U_w the velocity in the wake, ρ the water density, U_∞ the velocity far upstream of the disc and U_d the velocity at the disc location. From equation (1) and the definition of the wake velocity as $U_w = (1 - 2a)U_\infty$, the force on the fluid can be defined as follows:

$$Force = (p_d^+ - p_d^-)A_d = 2\rho A_d U_\infty^2 a(1 - a) \tag{2}$$

The actuator disc area (m^2) A_d is equivalent to the area swept by the turbine blades. By normalizing this force, one can introduce a standard non-dimensional quantity called the coefficient of thrust C_t (Burton, et al., 2008):

$$C_t = \frac{Force}{\frac{1}{2}\rho A_d U_\infty^2} = 4a(1 - a) \tag{3}$$

In the field of physical scale modeling the coefficient C_t is related to disc porosity (Harrison, et al., 2009). The induction factor a is a dimensionless quantity, ranging from 0 to 1, which represents the strength of the reduction in fluid velocity. From equation (3), the force on the fluid induced by the presence of a turbine, also called the thrust force $\overrightarrow{F_t}$, can be expressed as follows:

$$\begin{cases} \overrightarrow{F_t} = -\frac{1}{2}\rho A_d C_t(|\overrightarrow{v_\infty}|\overrightarrow{v_\infty}).\vec{n} = -\frac{1}{2}\rho A_d C_t \begin{cases} (|u_\infty|u_\infty).(\vec{n}.\overrightarrow{e_x}) = \overrightarrow{F_{t,u}} \\ (|v_\infty|v_\infty).(\vec{n}.\overrightarrow{e_y}) = \overrightarrow{F_{t,v}} \end{cases} \\ \vec{n} = unitary\ normal\ vector\ to\ the\ disc\ surface \end{cases} \tag{4}$$

The force being concentrated at the actuator disc, the power extraction from the fluid is equivalent to the rate of work done by the force ($Work = Force \times U_d$). According to the definition of the induction factor, the extracted power is given by

$$Power = Force \times U_d = 2\rho A_d U_\infty^3 a(1 - a)^2 \tag{5}$$

The induction factor can also be linked to the power coefficient C_{power}, which has the value of the ratio between extracted power and available power, and can be expressed as follows:

$$C_{power} = \frac{Power}{\frac{1}{2}\rho A_d U_\infty^3} = 4a(1 - a)^2 \tag{6}$$

Equations (4) and (6) constitute the core of the actuator disc concept (Burton, et al., 2008). The limit of this theory is set for a value of $a \leq \frac{1}{2}$ above which the velocity in the wake U_w becomes zero, or even negative. Beyond this limit the momentum theory needs to be adapted to be relevant (Burton, et al., 2008).

Draper et al. (2009), Lalander & Leijon (2009) and Bryden & Couch (2007) used the actuator disc concept in 2D large scale models in order to assess the power available in a realistic flow. However, as 2D models are depth integrated, the implemented thrust force is, therefore, vertically uniform over the water column. This brings confusion in its physical meaning since it can be equally regarded as a drag force (Draper, et al., 2009) or an additional shear stress (Lalander & Leijon, 2009).

As a consequence, the vertical flow behavior such as the relation between water column height and corresponding drag coefficient (Sutherland, et al., 2007), vertical flow bypassing of the device or distinction between bottom friction and energy extraction (Karsten, et al., 2008), are misrepresented and thus wrongly estimated. Kawase & Thyng (2009) highlighted, through a 3-D model using the additional bottom shear stress method, the importance of integrating baroclinic dynamics in the simulation to fully assess the turbine yield (Kawase & Thyng, 2009). The actuator disc concept has been successfully applied to 3D CFD wake models by Harrison et al. (2009) and Sun & Bryden (2008). Thanks to the high resolution of CFD methods and despite the assumption that TCTs can be assimilated to non-rotating objects, the actuator disc concept seems to accurately compute the wake decay (Harrison, et al., 2009; Sun, et al., 2008). Unfortunately, because of their high grid resolution and significant computational cost, CFD models cannot be used for simulating realistic flows with large spatial coverage and complex bathymetry and forcing. Since TCT array optimization has to account for a wide range of scales going from wake interactions to large hydrodynamic impacts, ocean-circulation type models would be preferred to CFD models.

Réthoré et al. (2009) and El Kasmi et al. (2008) raised the problem of applying the actuator disc concept to 3D ocean-circulation models. Indeed, the grid resolution and the turbulence closure models used in most of the 3D large-scale models set an arbitrary threshold of time and scale below which flow fluctuations are considered as turbulence. Since the length and time scales of the turbulence induced by a turbine are several times smaller than the length and time scales of turbulence considered by the turbulence closure models of large-scale models, correction terms need to be injected into the closure model in order to account for the turbulence activity induced by the turbine (Réthoré & Sorensen, 2008; Kasmi & Masson, 2008; Rados, et al., 2009). Moreover, it is even more important to account for turbine induced turbulence since, in most realistic cases, the limit value of $a \leq \frac{1}{2}$ will be exceeded and, accordingly, device induced turbulences will have a major role in the spatial wake decay (Roc, et al., 2010; Roc, et al., 2011). From a physical point of view this threshold marks the point where the wake becomes turbulent and where the flow separates at the disc's edge and spreads radially, generating a virtual radial expansion of the rotor disc (Burton, et al., 2008). Those phenomenon combined with the proximity of the free-surface and the sea-bottom, above and beneath the rotor disc, may also lead to an enhanced horizontal expansion of the virtual rotor disc (Daly, et al., 2010). The flow separation is characterized by a slow moving region of low pressure straight after the disc and a fast moving region of high pressure at the front of the disc and around the edge of the device as the fluid surges then flows around the turbine. The induced static pressure drop cannot be balanced by the kinetic energy; therefore the energy loss is compensated by the mixing process taking place in the turbulent wake (Burton, et al., 2008). By analogy with a flat plate, this slow moving area shall be referred to as the stagnation area even though part of the flow still passes through the rotor-disc (area swept by the turbine blades). Furthermore, this phenomenon is amplified by the blockage effect inherent to constrained flows (Whelan, et al., 2007). In summary using the actuator disc concept in large-scale numerical models without adapting the models to account for the turbine induced turbulence occurring in the near wake region would lead to a misrepresentation of the wake recovery and impacts in realistic scenarios.

2.2. Accounting for Turbulence Perturbations

Although empirical approaches have been attempted by Buhl (2005) and Whelan (2007) to adapt the actuator disc theory beyond its limit of validity by artificially enhancing the thrust

coefficient (Buhl, 2005; Whelan, et al., 2007), empirical parameterizations of the thrust coefficient present difficulties for developing a TCT array optimization tool. Such empirical approaches require large set of data for almost every scenario and, most importantly, miss the turbulence aspect of the problem. In order to improve the discrepancies in the near wake performance, and by extension wake recovery, of large-scale simulations it may be important to recognize that the fluid passing through a rotor results in a local disturbance of the turbulence equilibrium (Blunden & Bahaj, 2007).

From the point of view regarding turbulence, the presence of a turbine in a flow generates shear, itself created by the velocity gradient of the wake. This type of turbulence is handled by the turbulence production term P common to any 2-equation turbulence closure model used in large-scale models. On the contrary, blade root and tip vortices as well as some of the blade shed vortices induce turbulence downstream of the device but are not accounted for in closure models as an active contribution in the turbulent dynamics (Réthoré, et al., 2009). Likewise, after breaking down a few rotor diameters beyond the turbine, wake rotational motion and vortices that also contribute to the wake dissipation but are not accounted for in closure models (Réthoré, et al., 2009). In the respective areas of wind turbine and forest canopy research, Sanz (2003) and Rethore et al. (2009) proposed a technique to account for these turbine induced turbulences. It consists in adding a source term, P_P, into the turbulent kinetic energy (TKE) transport equation of 2-equation turbulence closure models (Sanz, 2003). P_P is defined as being proportional to the cube of flow-velocity in the turbulent kinetic energy (TKE) and only active at the rotor-disc location.

$$P_p \propto \|\vec{v}\|^3 \tag{7}$$

Furthermore, turbines (or porous discs) transfer some kinetic energy harnessed from larger scale turbulence into finer scale turbulence (Harrison, et al., 2009; Réthoré, et al., 2009; Kasmi & Masson, 2008), perturbing the natural turbulence cascade described by Kolmogorov (Kolmogorov, 1941). In contrast with porous discs, turbines extract part of this transferred energy as mechanical power (Réthoré, et al., 2009). This phenomenon is referred as the "short-circuiting of the turbulence cascade" (Sanz, 2003; Réthoré, et al., 2009; Kasmi & Masson, 2008; Rados, et al., 2009). Sanz (2003) and Rethore et al. (2009) proposed to account for this energy transfer by adding a sink term P_d in the TKE transport equation of 2-equation turbulence closure models. P_d is defined as being proportional to the flow-velocity multiplied by the TKE and only active at the rotor-disc location.

$$P_d \propto -\|\vec{v}\|.k \tag{8}$$

At the same time, the turbulence field present in the near wake will exhibit a reduced spectrum of length scales as it is partially generated by direct fluid interactions with the rotor (or porous disc) (Bryden & Melville, 2004; Bryden & Couch, 2004). In the area of wind turbine research, Kasmi & Mason (2008) and Rados (2009) proposed to account for this length-scale transfer by injecting a new time-scale related to the energy transfer rate from large to small-scale turbulence in the turbulent length-scale (TLS) transport equation of 2-equation turbulence closure models. Accordingly, they added to the TLS transport equation of 2-equaton turbulence closure models, at the rotor-disc location, an extra term, P_ψ, as described by Chen & Kim (1987). P_ψ is defined as being proportional to the quadratic production of TKE by shear and only active at the rotor-disc location.

$$P_\psi \propto P^2 \tag{9}$$

6

The thrust force (4) combined with the three terms of the turbulence corrections (Eq. (7), (8) and (9)) compose the theoretical core of the present TCT representation method.

3. TCT Representation & Modeling

3.1. Description of ROMS

As mentioned in the introduction, ROMS has been chosen as the base modeling system to be adapted in this work. The key feature of ROMS is its ability to simulate realistic flow scenarios in a spatial reference frame of sufficient scale within a reasonable computational time period. It can be described as a 3-D, split-explicit, free-surface, terrain-following, hydrostatic primitive equation oceanic model (Shcheptkin & Mc Williams, 2005). Several numerical features such as the C-Arakawa staggered grid and the predictor-corrector scheme used in ROMS to improve its accuracy and computational speed make additional implementations very complex. It is worth noticing that, for the sake of clarity, the present work has been performed using an orthonormal horizontal grid with uniformly distributed sigma levels. Meso-scale models such as ROMS are currently the only models capable of providing simulations on the spatial scales necessary to bring a pertinent answer to such a complex and interdependent question as the TCT layout optimization.

As in most numerical models of oceanic circulation, ROMS applies simplifications regarding the three-dimensionality of physical quantities. For example, the hydrostatic assumption implies that the vertical motions can be derived only from the mass-conservation equation instead of explicitly resolving the full vertical momentum equation, making any vertical rotational motion impossible to simulate. In the same manner, vertical shear is assumed to be the dominate component and thus turbulent quantities vary mostly along the vertical (Umlauf & Burchard, 2005). As a result of these two assumptions, a splitting between horizontal and vertical resolutions is allowed in ROMS and parameterizations are required for sub-grid mixing processes such as momentum mixing and turbulence. In ROMS, vertical mixing and turbulence transport are computed via two equation turbulence closure schemes, whereas all the horizontal sub-grid mixing processes are encapsulated in an eddy-viscosity (Haidvogel & Beckmann, 1999) scheme. The turbulence correction terms presented in §2.2 have been implemented in the Generic Length Scale (GLS) closure model (Umlauf, et al., 2003) in order to permit the user to choose any 2-equation turbulence closure model (i.e. $k - \psi$, $k - kl$, $k - \omega$). These schemes generally possess one transport equation for the TKE $(m^2.s^{-2})$ and one transport equation for a chosen GLS related to the turbulent energy dissipation.

According to the assumptions describe above, the momentum equation system of ROMS can be expressed as:

$$\begin{cases} \frac{\partial u}{\partial t} + \vec{v}.\nabla u - fv = -\frac{\partial \varphi}{\partial x} - \frac{\partial}{\partial z}\left(-K_M \frac{\partial u}{\partial z} - v\frac{\partial u}{\partial z}\right) + A_M \left(\frac{\partial^2 \bar{u}}{\partial x^2} + \frac{\partial^2 \bar{v}}{\partial y^2}\right) \\ \frac{\partial v}{\partial t} + \vec{v}.\nabla v + fu = -\frac{\partial \varphi}{\partial y} - \frac{\partial}{\partial z}\left(-K_M \frac{\partial v}{\partial z} - v\frac{\partial v}{\partial z}\right) + A_M \left(\frac{\partial^2 \bar{v}}{\partial x^2} + \frac{\partial^2 \bar{u}}{\partial y^2}\right) \\ \frac{\partial u}{\partial x} + \frac{\partial v}{\partial y} + \frac{\partial w}{\partial z} = 0 \\ \frac{\partial \varphi}{\partial z} = -\frac{\rho g}{\rho_0} \end{cases}$$

(10)

In this set of equations, A_M represents the horizontal eddy viscosity and K_M the vertical viscosity

$$K_M = c\sqrt{2k}\,l\,S_M \tag{11}$$

where k is the turbulent kinetic energy (TKE) per unit mass, l is the length scale related to size of eddies that dominate the mixing, c is the stability function of Canuto et al. (2001) and S_M is a stability function defined by Kantha and Clayson (1994). The dynamics of k and l are computed in ROMS through a GLS closure model. The GLS closure model of ROMS can be formulated as:

$$\left\{\begin{array}{l} \dfrac{\partial k}{\partial t} + \bar{\bar{v}}.\nabla k = \dfrac{\partial}{\partial z}\left(\dfrac{\nu_t}{\sigma_k}\dfrac{\partial k}{\partial z}\right) + P + B - \varepsilon \\[2mm] \dfrac{\partial \psi}{\partial t} + \bar{\bar{v}}.\nabla \psi = \dfrac{\partial}{\partial z}\left(\dfrac{\nu_t}{\sigma_\psi}\dfrac{\partial \psi}{\partial z}\right) + \dfrac{\psi}{k}(c_1 P + c_3 B - c_3 \varepsilon F_{wall}) \\[2mm] \varepsilon = \left(c_\mu^0\right)^{3+\frac{p}{n}} k^{3-2+\frac{m}{n}} \psi^{-\frac{1}{n}}\,;\ \psi = \left(c_\mu^0\right)^p k^m l^n \end{array}\right\} \tag{12}$$

Here σ_k stands for the turbulent Schmidt number, σ_ψ the turbulent Schmidt number for ψ, ν_t vertical turbulent diffusivity, ε the TKE dissipation, ψ a generic parameter and l is the length scale of turbulence. P represents the production of TKE by shear, B represents the production of TKE by buoyancy and $c_1, c_2, c_3, c_\mu^0, m, n, p$ is a parameterization set. $c_1, c_2, c_3, c_\mu^0, m, n, p, \sigma_k, \sigma_\psi$ as well as the wall proximity function F_{wall} are parameters and coefficients linked to the Generic Length Scale (GLS) formulation for two-equation turbulence closure models. Here, for the sake of versatility, the k-ω closure model (where ω is the specific dissipation (s^{-1})) has been chosen since it is best suited for realistic oceanic situations and simulations with coarse resolution in the mixed layer (Umlauf, et al., 2003) (Eq. (12)), therefore $c_1 = 0.555$, $c_2 = 0.833$, $c_3 = -0.6$, $c_\mu^0 = 0,5477$, $m = 1/2$, $n = -1$, $p = -1$, σ_k=2.0 and $\sigma_\omega = 2.0$ (Umlauf & Burchard, 2001).

3.2. Model Modifications

As discussed in §2, from a regional scale standpoint, the hydrodynamic perturbations of TCTs can be split in two main components: the momentum balance as represented by the actuator theory (Eq. (13)) and the turbulence balance which will be accounted for in this work by appropriate turbulence-correction terms (Eq. (19)). In the development presented here, several simplifications are made. Firstly, the device supporting structure and its related effects on the flow are neglected. Secondly, the rotor-disc orientation is taken to be normal to the incoming flow. Thus, the retarding force $\overrightarrow{F_t}$ is always applied in the same direction as the flow, thus equation (4) can be simplified to:

$$\overrightarrow{F_t} = -\frac{1}{2}\rho A_d C_t(|u_\infty|u_\infty).\vec{n} \tag{13}$$

Accordingly, at the rotor-disc location and within the current frame of simplifications, ROMS momentum equation systems (Eq. (10)) are modified as follows:

$$\left\{\begin{array}{l} \dfrac{\partial u}{\partial t} + \vec{v}.\nabla u - fv = -\dfrac{\partial \varphi}{\partial x} - \dfrac{\partial}{\partial z}\left(-K_M\dfrac{\partial u}{\partial z} - v\dfrac{\partial u}{\partial z}\right) + A_M\left(\dfrac{\partial^2 \bar{u}}{\partial x^2} + \dfrac{\partial^2 \bar{v}}{\partial y^2}\right) + F_t \\[2mm] \dfrac{\partial v}{\partial t} + \vec{v}.\nabla v + fu = -\dfrac{\partial \varphi}{\partial y} - \dfrac{\partial}{\partial z}\left(-K_M\dfrac{\partial v}{\partial z} - v\dfrac{\partial v}{\partial z}\right) + A_M\left(\dfrac{\partial^2 \bar{v}}{\partial x^2} + \dfrac{\partial^2 \bar{u}}{\partial y^2}\right) \\[2mm] \dfrac{\partial u}{\partial x} + \dfrac{\partial v}{\partial y} + \dfrac{\partial w}{\partial z} = 0 \\[2mm] \dfrac{\partial \varphi}{\partial z} = -\dfrac{\rho g}{\rho_0} \end{array}\right\} \tag{14}$$

One can notice that $\overrightarrow{F_t}$ has been defined as a function of the unperturbed flow speed $\overrightarrow{u_\infty}$ although this force is applied at the location of the turbine blades. Therefore, in order to account for the real nature of the flow perturbation as well as for the sake of implementation, $\overrightarrow{F_t}$ should be defined as function of the flow velocity at the disc location $\overrightarrow{u_d}$. The unperturbed flow speed, $\overrightarrow{u_\infty}$, can be expressed as follows:

$$u_\infty = \frac{u_d}{(1-a)} \tag{15}$$

In this manner the thrust force $\overrightarrow{F_t}$ can be rewritten as follows:

$$\overrightarrow{F_t} = -\frac{1}{2}\rho A_d C_t \frac{|u_d|u_d}{(1-a)^2}.\vec{n} \tag{16}$$

As shown in Hansen, et al. (2000), equations (3) and (6) lead to the following expression of the induction factor:

$$a = \frac{1}{2}\left(1 - \sqrt{1-C_t}\right) \tag{17}$$

Using Eq. (3) and (17), Eq. (16) then becomes:

$$\overrightarrow{F_t} = -\frac{1}{2}\rho A_d \left(4 \times \frac{1-\sqrt{1-C_t}}{1+\sqrt{1-C_t}}\right)|u_d|u_d.\vec{n} = -\frac{1}{2}\rho A_d C|u_d|u_d.\vec{n} \tag{18}$$

where C is related to C_t through Equation (25).

As for the turbulence correction terms described in §2.2, they required some transformations before being injected in the GLS closure of ROMS. Indeed in their respective sources, P_d, P_p and P_ψ have been developed for either $k-\varepsilon$ or $k-\omega$ closure models and therefore needed to be adapted to fit within the GLS framework. In this way, the user has the option to switch to any kind of 2-equation closure model on demand. Accordingly the three turbulence correction terms are expressed as follows:

$$\begin{cases} P_k = C_p \dfrac{u^3}{\Delta x} - C_d \dfrac{u.k}{\Delta x} = P_p - P_d \\[2mm] P_\psi = C_\psi \dfrac{P^2}{\varepsilon} \; ; \end{cases} \tag{19}$$

And, at the rotor-disc location, are injected in the GLS closure of ROMS (Eq.(12)).

$$\left.\begin{cases} \dfrac{\partial k}{\partial t} + \vec{\bar{v}}.\nabla k = \dfrac{\partial}{\partial z}\left(\dfrac{v_t}{\sigma_k}\dfrac{\partial k}{\partial z}\right) + P + B - \varepsilon + P_k \\[3mm] \dfrac{\partial \psi}{\partial t} + \vec{\bar{v}}.\nabla \psi = \dfrac{\partial}{\partial z}\left(\dfrac{v_t}{\sigma_\psi}\dfrac{\partial \psi}{\partial z}\right) + \dfrac{\psi}{k}(c_1 P + c_3 B - c_3\varepsilon F_{wall} + P_\psi) \\[3mm] \varepsilon = \left(c_\mu^0\right)^{3+\frac{p}{n}}k^{3-2+\frac{m}{n}}\psi^{-\frac{1}{n}} \; ; \; \psi = \left(c_\mu^0\right)^{p}k^m l^n \end{cases}\right\} \tag{20}$$

The detailed implementation into ROMS of the present method can be found in Appendix 1: Numerical Implementation.

3.3. Test Case Description & Benchmarking

In order to validate the capability of the proposed TCT modeling method, a comparison between physical scale model and numerical model results has been conducted. The reference physical scale model is described by Myers and Bahaj (2010) and was used by Harrison *et al.* (2009) as reference data to evaluate the performance of CFD simulations. The experimental features of this flume test are:

- A rectangular channel with a 21000 mm long (L), 1350 mm wide (l) and 300 mm deep (h) working section
- Turbine represented by a 100 mm diameter (d) perforated disc with a porosity corresponding to C_t=0.86
- A constant, depth-averaged inflow of 0.33 m/s whose vertical profile closely matches a (1/7)th power law.
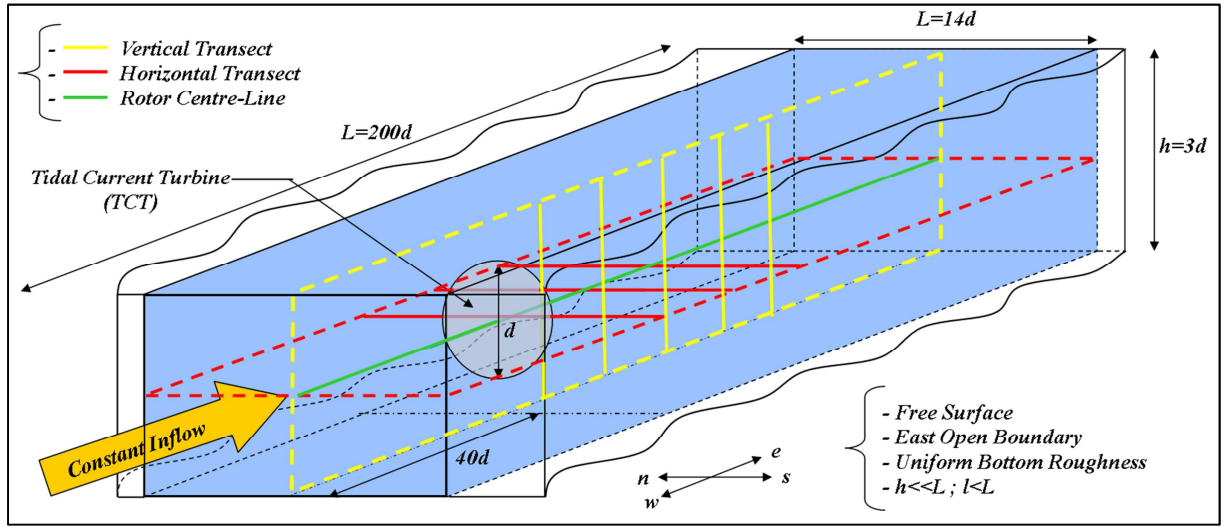- Bottom roughness length of approximately z_0=8 mm

Figure 2: Idealized channel, centre-line, profile and transect locations. This conceptual diagram represents the validation test geometry and dimensions as well as the locations where measurements have been taken.

The numerical grid used for the flume simulation has 420 grid cells in the stream wise direction (equivalent to $\Delta x = 0.05m$ ($\frac{D}{2}$)), 67 grid cells in the cross-stream direction (corresponding to $\Delta y \approx 0.02m$ ($\frac{D}{5}$)) and 30 vertical levels in the grid which are linearly distributed in sigma space in the vertical (equivalent to $\Delta z = 0.01m$ ($\frac{D}{10}$)). Specific grid features for the grid dependency tests are described in §4.1. A constant, depth-averaged inflow of 0.33 m/s is imposed at the upstream channel boundary and the free-surface elevation at the downstream boundary is held at 0 m. A free-surface radiation condition, 2D momentum Flather condition and 3D momentum radiation condition are applied on the upstream open boundary; a free-surface clamped condition, 2D momentum reduced-physics condition and 3D momentum radiation condition are used for the downstream open boundary (Carter & Merrifield, 2007); free-slip conditions are applied on the lateral walls. The model ran until the results indicated that a steady state had been achieved, namely when model averages of velocity, TKE and free surface elevation, taken at the device location, varied by less than 0.1% from one time step to the next. The time step used for the simulation meets CFL (Courant-Friedrichs-Lewy) criterion. It has been verified that using a shorter time step does not change the steady state

solution. The simulations have been computed in parallel on 8 processors of 2.5 GHz clock-rate using Message Passing Interface (MPI) libraries. With this set-up, on average, it takes around 6 minutes for the simulations to reach a steady state.

Prior to model-data comparisons, the simulation results had to be interpolated on a regularly spaced orthogonal grid equivalent to that for which observations were collected. The preferred metric for validation was turbine wake recovery. A conventional method to characterize wake recovery is the rotor velocity deficit $U_{deficit}$ (Eq. (21)). This non-dimensional number is a function of the ratio between free-stream flow velocity U_∞ and the wake velocity U_w, both measured at equivalent vertical and lateral locations in the channel. TKE and the turbulence intensity (TI) have been chosen as the benchmark quantity for turbulence behaviors (Eq.(29)).

$$U_{deficit} = 1 - \frac{U_w}{U_\infty} \tag{21}$$

$$TI = \frac{\sqrt{\frac{2}{3}k}}{U} \tag{22}$$

In order to examine the accuracy of the simulation in three dimensions, horizontal and vertical transects have been made at different locations downstream of the turbine (Figure 2). Diagnostic focus is placed on velocity deficits along the rotor-centre line (Figure 4, Figure 5, Figure 6 and Figure 7) although spatial distributions are also examined (Figure 8 and Figure 9). The centre line is defined as the horizontal line normal to the rotor disc passing through its centre. Notice that both reference flume conditions (Figure 3) and velocity deficits along the centre line (Figure 7) are taken from Myers and Bahaj (2010) whereas both reference velocity deficit and TKE horizontal transects and vertical profiles (Figure 6, Figure 8, Figure 9, Figure 10, and Figure 12) are taken from the appendix of Harrison *et al.* (2009). Statistical approaches have been used to assess the accuracy of the numerical method used to replicate the experimental results. The correlation between the reference and simulated data has been investigated by using the standard Pearson product-moment correlation coefficient r. The error of magnitude between the physical experiment and simulated values is estimated by the root mean square error percentage normalized by the amplitude of the considered quantity $\%_{Nrmse}$ (Eq. (23)).

$$\%_{Nrmse} = \frac{\sqrt{\frac{1}{n}\sum_{i=1}^{n}(q_i - \bar{q})^2}}{q_{max} - q_{min}} \times 100 \tag{23}$$

The first step of the simulation phase was to reproduce the flume conditions without any device deployed in order to obtain the best fit with the experimental data. Several initial inputs, such as the bottom roughness height and the minimum value of specific TKE, had to be set empirically. Notice that discrepancies in model data comparisons arise from locations where the experimental data deviate from smooth profiles (Figure 3). The values of correlation coefficients and error percentages for both velocity and TI reached for this simulation (namely $r = 0.88$ with $\%_{Nrmse} \cong$ 3.5% for the velocity and $r = 0.94$ for TI $\%_{Nrmse} \cong 10\%$) give insight into what level of confidence can be expected for the simulated results but also on the overall uncertainty carried by the physical experiment data for both momentum and turbulence quantities. Additionally, using a logarithmic analysis of uncertainty propagation applied on the Eq. 19, one can expect $\%_{Nrmse} \cong 13\%$ as a satisfying error level for TKE values derived from TI measurements.
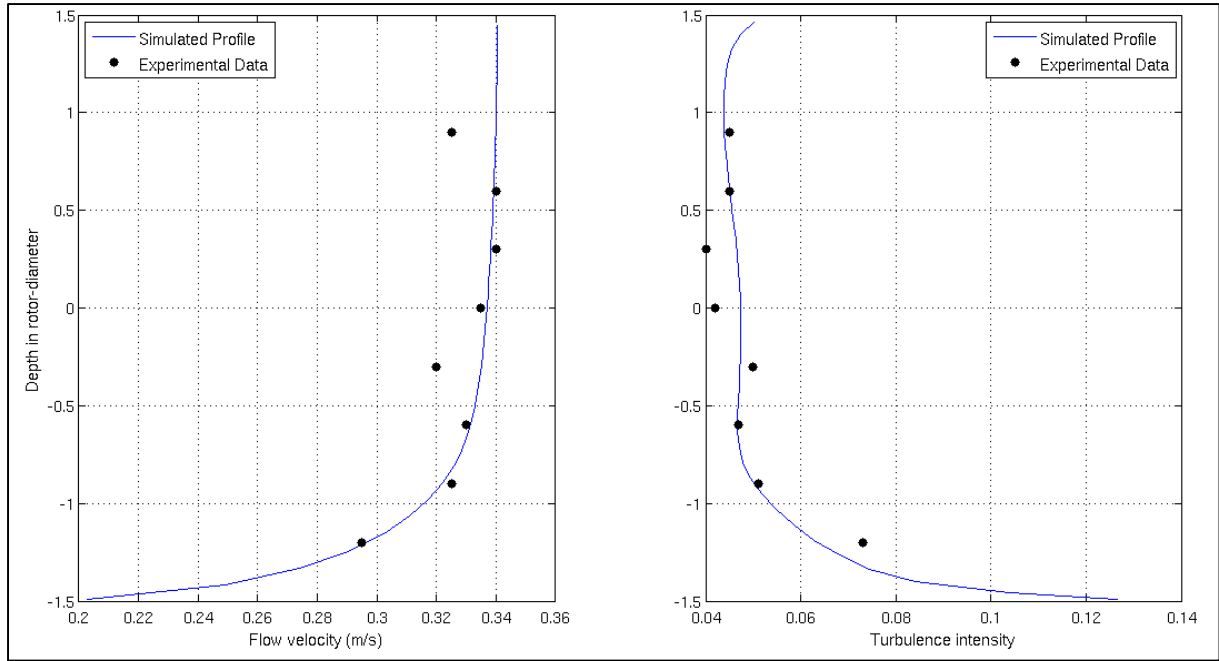
Figure 3: Initial conditions – physical experiment data (points) versus simulated results (solid lines). The left hand graph displays velocity profiles and the right hand graph turbulence intensity profiles.

4. Numerical Tests & Validation

4.1. Grid Dependency

Grid-dependency tests have been performed to verify that, as the grid resolution gets finer and finer, the simulation converges toward an asymptotic solution. In addition, these tests identify minimal grid resolutions that will render the turbine representation results relatively insensitive to the resolution and so grid independent. Additionally, not meeting those criteria would reveal inconsistency in the numerical implementation itself. Horizontal and vertical resolution tests have been conducted independently. In the ROMS model, changing the number of sigma levels implies re-tuning several input parameters, such as the bottom roughness and/or the minimum value of specific TKE in order to fit with the initial conditions imposed by the reference experiment (Figure 3). This imposed re-setting phase, although quite time consuming, is required in order to match the observed input conditions. Centre line velocity deficits are presented for expediency sake as these results have been confirmed to be representative of those observed by examining vertical profiles and horizontal transects.
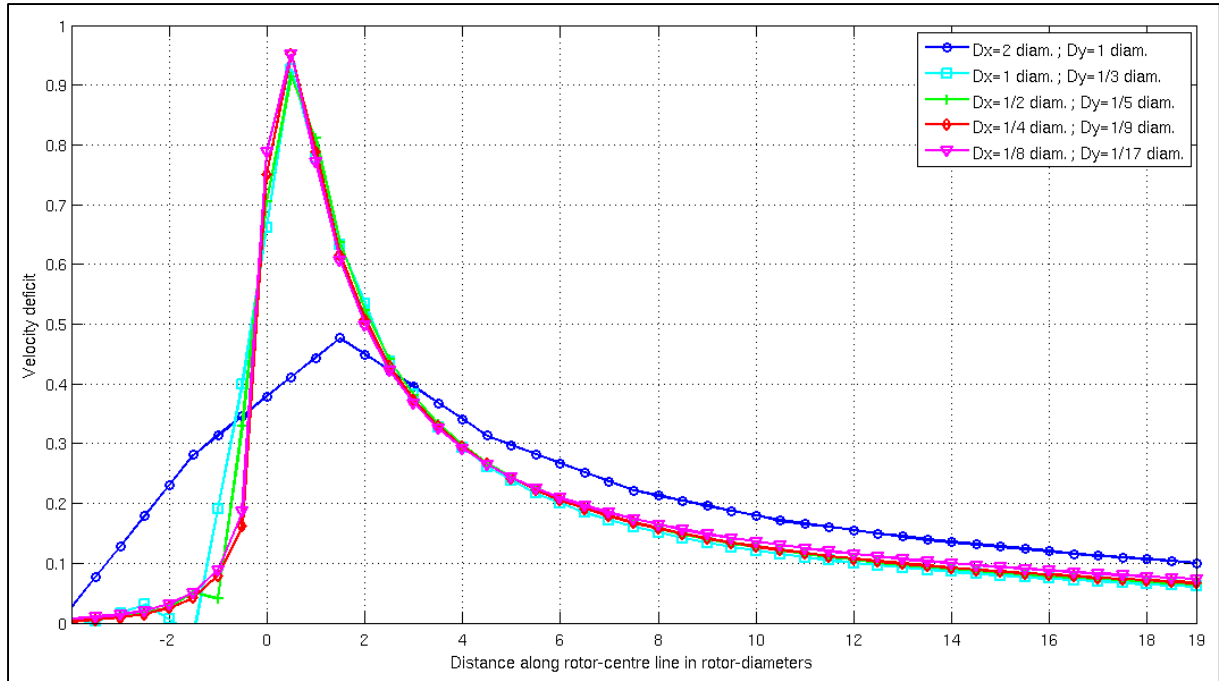
Figure 4: Velocity deficits along centre-Line – Horizontal-resolution dependency test. Each marked line is linked to a different horizontal grid resolution for the same simulation (blue to red correspond to coarse to fine resolution). Notice that all solutions converge toward an asymptotic solution.

Figure 4 gives results of velocity deficits where Δx and Δy vary simultaneously. Originally the intention was to keep the same ratio $\frac{\Delta y}{\Delta x}$ (i.e. $\frac{1}{2}$) as it appeared to be a reasonable criterion for grid generation. However, experience has shown the implementation gives better results for odd numbers of lateral cells. Using an even numbers leads to averaging of the rotor centre deficit peak and thus a misrepresentation of the centre-line wake decay. Consequently, the horizontal spacing ratio has been kept as constant as possible in the light of the odd number requirement on lateral cells. Figure 4 clearly shows that simulations converge toward an asymptotical solution as the grid resolution is refined. One can also observe that after a resolution of $\Delta x = \frac{1}{4}D$; $\Delta y = \frac{1}{9}D$ (red line with diamonds in Figure 4) the difference in wake decay on the simulation is almost imperceptible. As for the minimal resolution, in comparison with the error level that can be expected from the code (i.e. §0), a resolution of $\Delta x = 1D$; $\Delta y = \frac{1}{3}D$ (light-blue line with squares in Figure 4) and finer would be optimum since its deviation with the asymptotical value is less than 5%$_{Nrmse}$. Above this limit, coarser resolution leads to information loss and results in an unsatisfactory deviation with the asymptotical value as, for instance, a resolution of $\Delta x = 2D$; $\Delta y = 1D$ leads to a deviation of 15%$_{Nrmse}$ with the optimal solution (blue line with circles in Figure 4).
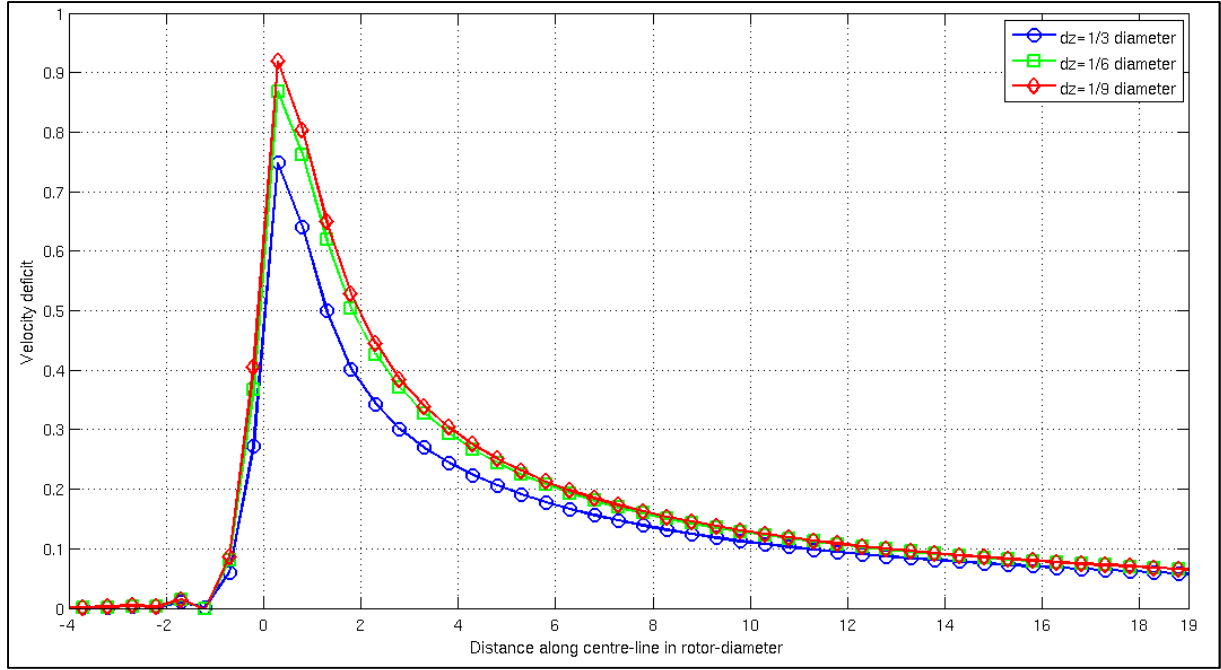
Figure 5: Velocity deficits along centre-line – Vertical-resolution dependency test. Each marked line is linked to a different vertical grid resolution of the same simulation (blue to red correspond to coarse to fine resolution) and they all converge toward an asymptotic solution.

In the same manner as Figure 4, Figure 5 shows results of velocity deficits but, in this case, for varying Δz. As can be determined by the discussion in the previous paragraph, the results presented in this section have been performed with a horizontal resolution of $\Delta x = 1D$; $\Delta y = \frac{1}{3}D$. Owing to the practical reasons of re-setting stated previously, the figure does not display as many cases as Figure 4. Concerning the minimal resolution, an acceptable simulation (<5%$_{Nrmse}$) is reached with a $\Delta z = \frac{1}{6}D$ vertical-level resolution. It is worth noting that, in coastal applications where tidal turbines are likely to be sited, vertical resolution is unlikely to be a limiting feature. Indeed for a 3-D shallow-water numerical simulation, the number of vertical levels required to accurately catch vertical hydrodynamics would generally lead to a Δz finer than $\frac{1}{6}D$.

4.2. Validation against experimental data

Under the model development discussed in Appendix 1: Numerical Implementation, the potential free coefficients (i.e. C, C_d, C_p, C_ψ) have been assigned the values recommended in the published literature hence, the only parameter that needs empirical calibration is the eddy viscosity. In the present case, the eddy viscosity is calibrated against the horizontal expansion of the turbine wake and far-wake vertical profiles of TKE provided by Harrison *et al.* 2010 (Figure 6).
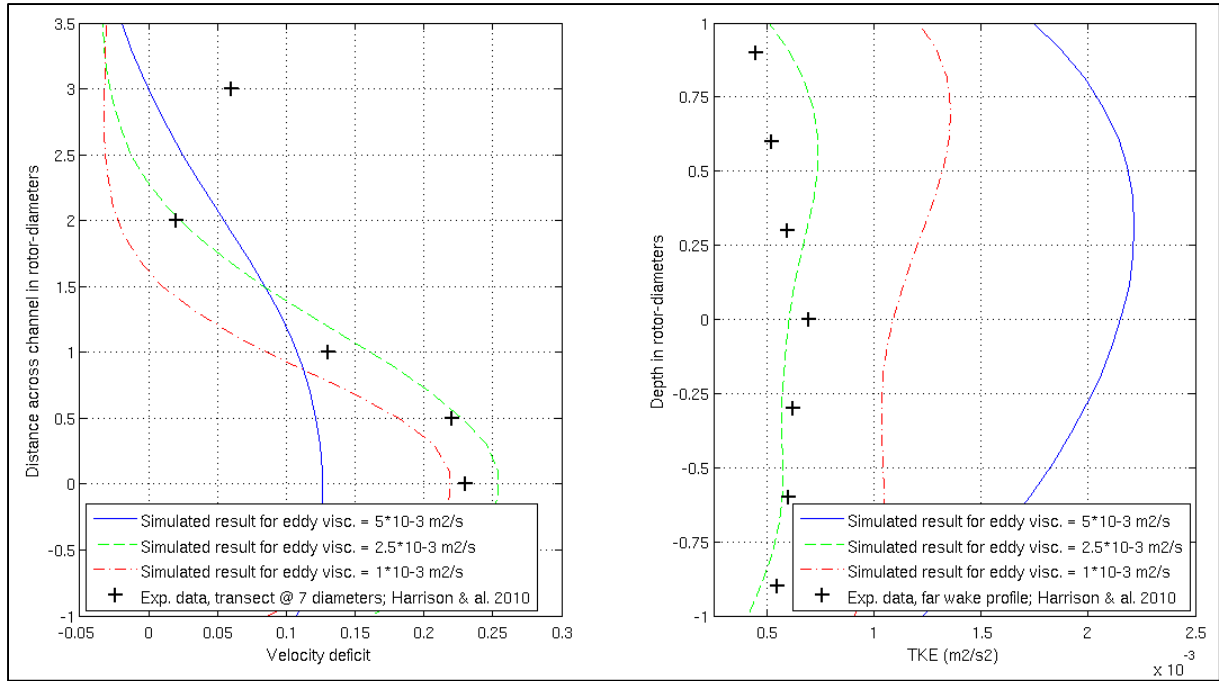
Figure 6: Eddy viscosity calibration figure showing horizontal transects of velocity deficits (left) & vertical profiles of TKE (right) at a distance of seven diameters downstream from the device. The experimental far-wake horizontal velocity and vertical TKE (black crosses) are used as benchmark for the eddy viscosity calibration; each type of lines (blue solid, green dashed and red dotted-dashed) represent simulated results of different eddy-viscosity values for the corresponding experimental data.

The left hand graph of Figure 6 shows horizontal transects of velocity deficit taken at seven diameters downstream of the device for various eddy viscosity values as well as the corresponding experimental data points. Predictably, increasing the eddy viscosity value used in the simulation leads to an increase in the lateral spread of the wake. The right hand graph of Figure 6 shows vertical profiles of TKE taken at 15 diameters downstream of the device for various eddy viscosity values as well as the corresponding experimental profile. Noticeably, increasing the eddy viscosity value used in the simulation leads to a non-linear variation of TKE, in other words, a non-linear variation of far wake turbulence level. An eddy viscosity of $2.5 * 10^{-3} m^2 . s^{-1}$ appears to give, in terms of horizontal wake expansion and far wake turbulence level, the optimum match with the experimental data. Nonetheless, there are some differences towards the channel wall boundaries which are thoroughly discussed further in this section.

These results give confidence in the calibration of the horizontal momentum dissipation in the simulation and the aptitude of the method for accurately simulating the flow perturbation induced by the device. The case with the deployed devices can now be investigated. Figure 7, Figure 8 and Figure 9 illustrate comparison of the velocity deficit between the reference flume-scale model and its equivalent numerical simulation obtained by the present TCT representation method. Figure 7 shows velocity deficits along the centre-line for a case where only the thrust force is considered (dashed line), a case where both thrust force and turbulence correction are included (solid line) and the experimental data (crosses).
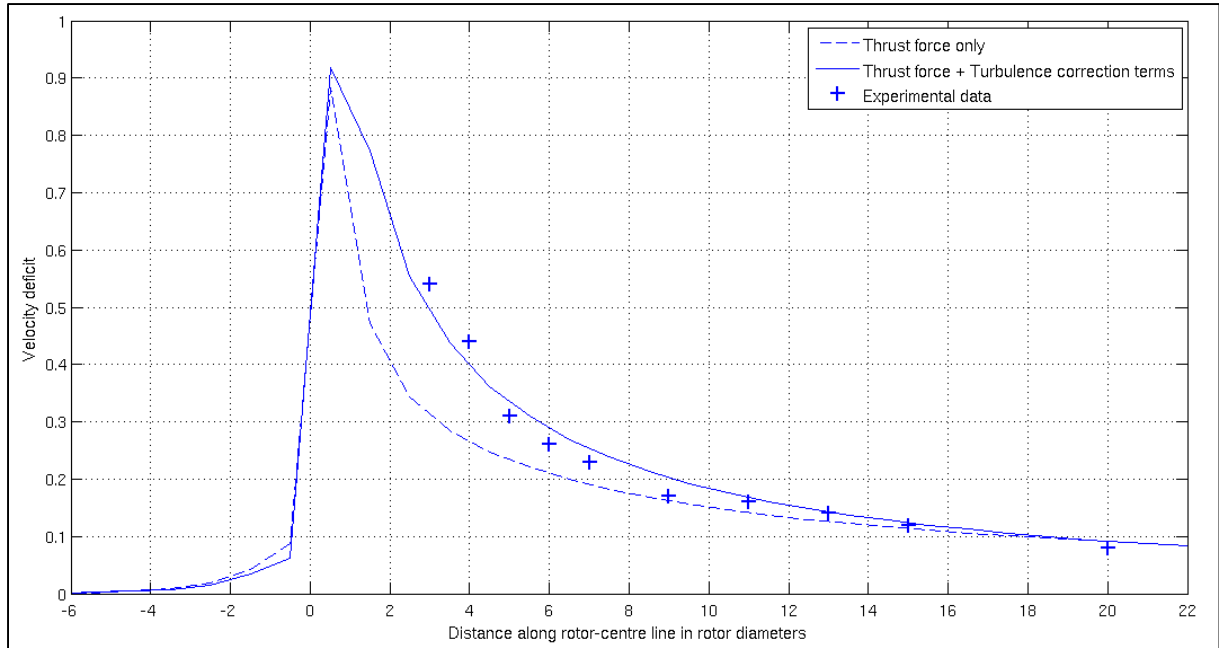
Figure 7: Plot of velocity deficits along centre-line demonstrating the effect of including turbulence correction terms. The experimental data is represented by the crosses. The corresponding simulation results which utilizes only the thrust force is shown with the dashed line and the full simulation accounting for both the thrust force and turbulence perturbations is presented with the solid line.

Accounting for the device-induced turbulence components in the numerical TCT representation appears to be necessary in large-scale simulations in which sub-scale turbulence phenomena are not fully and/or explicitly computed. Indeed Figure 7 illustrates the fact that, in large-scale models, only accounting for the momentum perturbation leads to a poor assessment of the wake recovery and that one way to reproduce accurately both the near and far wake recovery is to parameterize the non-linear turbulence perturbations generated by the near-wake turbulence-disequilibrium. By doing so, the match of velocity deficits along the rotor-centre lines between simulated and experimental data reaches a correlation coefficient of $r = 0.99$ and a normalized root mean square error percentage ($\%_{Nrmse}$) of 5.8%.

Figure 8 displays the simulated horizontal transects of velocity deficit taken along a median plane at different locations downstream of the device and the corresponding experimental transects upon which a comparison can be made. There is a strong correlation between the simulated transects and the experimental data ($r = 0.94$) although the highest disagreement occurs at the lateral extremity of the study area. The deviation of magnitude between simulated and experimental data does not reach the level of confidence expected ($\%_{Nrmse} = 12\%$) but the reduced discrepancy ignoring the points closest to the wall results in a value of 9.4%.
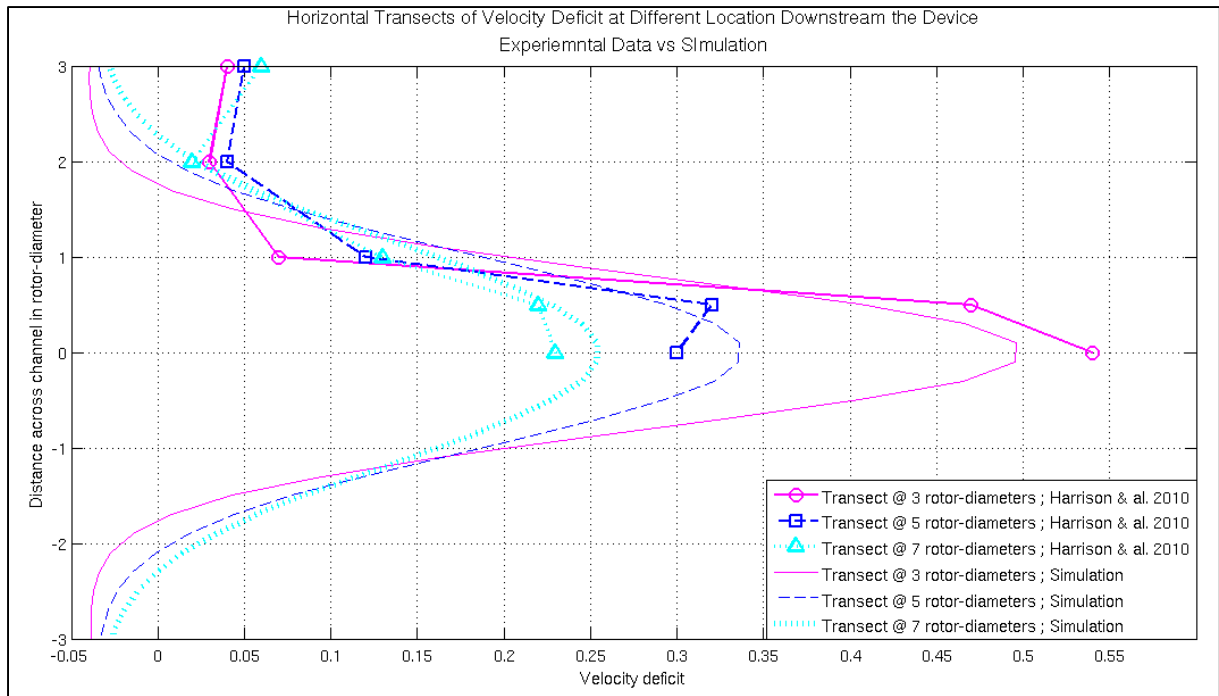
Figure 8: Horizontal transects of velocity deficits taken at different locations downstream to the device – Experimental data versus simulated results. Experimental transects (marked lines) are used as benchmarks to estimate the accuracy of their simulated equivalents (lines of matching colors and types).

This level of error can be attributed to two reasons. First the experimental data base being quite sparse (15 points) and spatially narrow (from 0D to 3D), any deviation from the data has high weight. Most importantly however is the obvious disagreement on the horizontal flow recovery of the outer-disc region. The simulation shows a slight acceleration of the flow for the region greater than 2 diameters away from the disc centre whereas the experiment data shows an apparent deceleration. While the source of this discrepancy is unknown, mass conservation requires an acceleration in part of the unblocked gaps in a partially blocked channel as observed in the simulations. The free slip condition imposed on the side walls of the simulation may lead to an improper allocation of this region of acceleration to the sidewall region.

Figure 9 displays vertical profiles of velocity deficit taken along a median plane at different locations downstream of the device for both simulation and experimental data. Comparison has been made between the simulation profiles and experimental data. In the same manner as the horizontal transects, a strong correlation between the simulation and the experiment ($r = 0.9$) is evident and the deviation of magnitude ($\%_{\mathrm{Nrmse}} = 8.1\%$) again does not quite meet the optimum level of confidence obtained for the initial case (i.e. §3.3.) although omission of the data points nearest the bottom boundary reduces this number to 6.8%.
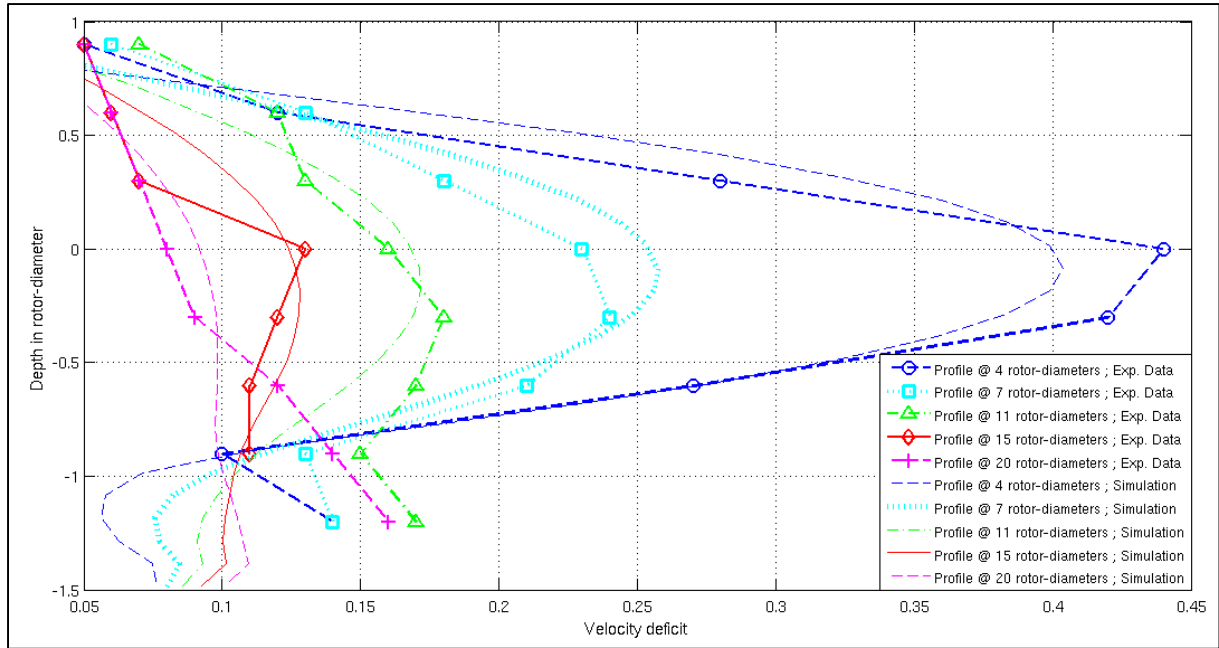
17

Figure 9: Vertical profiles of velocity deficits taken at different locations downstream to the device – experimental data versus simulated results. Experimental profiles (marked lines) are used as benchmarks to estimate the accuracy of their simulated equivalents (lines of matching colors and types).

The reasons mentioned in the previous paragraph to justify the discrepancies of the horizontal flow behavior could be also applied here, yet an additional explanation is worth discussion. At the current stage of development, the TCT module structure relies on the ROMS built-in "body force" implementation. Application of this option requires an a-priori definition of the thickness of the bottom and upper mixed layers within which the boundary layers and related mixing processes will be restrained.

One of the advantages of the present method and probably a unique feature within the existing meso-scale TCT models is the ability to simulate the turbulence perturbations induced by the devices on the flow. Self-evidently, the model does not explicitly resolve the sub-scale turbulence dynamics but does account for it, and it is important to understand the level of confidence in the results. Figure 10 and Figure 12 provide the required elements to answer this question by illustrating comparison of the turbulence features between the reference flume-scale model and its equivalent numerical simulation. It is worth noticing that the experimental values of TKE displayed in Figure 12 and 14 have been inferred from the turbulence intensity measurements (Harrison, et al., 2009) performed during the referenced flume test (i.e. §0., Eq. (22)). Figure 10 displays comparison of simulated and experimental vertical profiles of TKE taken along a median plane at different locations downstream of the device.
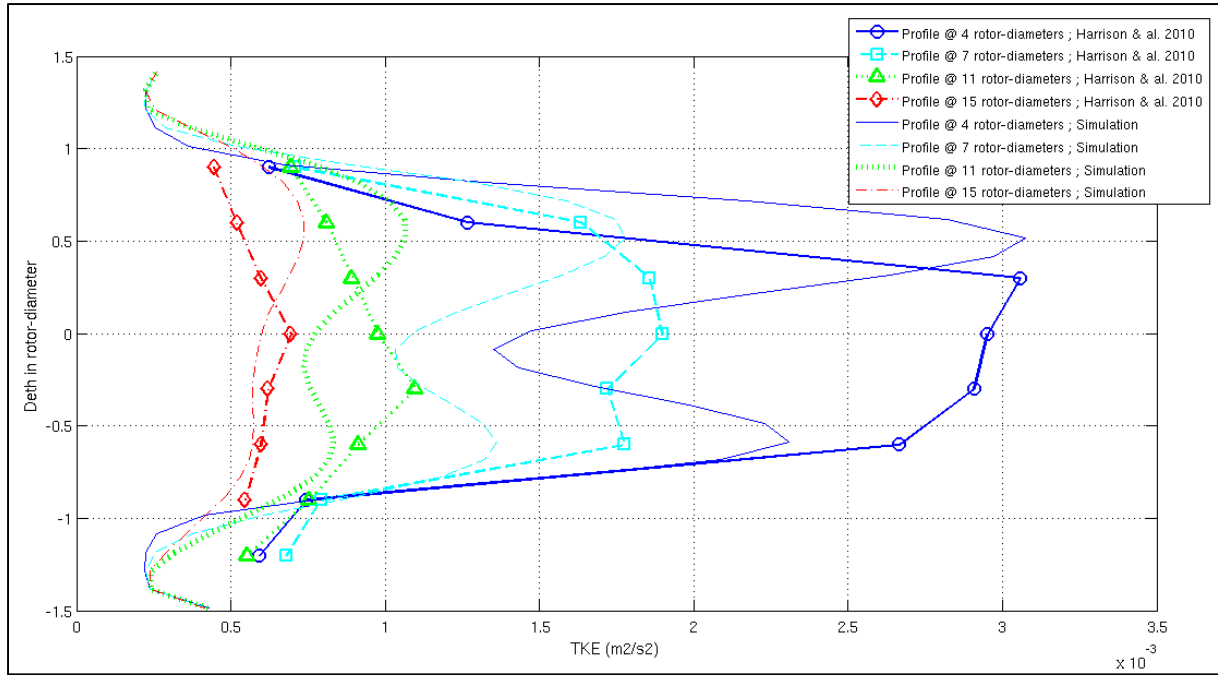
Figure 10: Vertical profiles of TKE at different locations downstream of the device – Experimental data versus simulated results. Experimental profiles (marked lines) are used as benchmarks to estimate the accuracy of their simulated equivalents (lines of matching color and type).

The vertical turbulent behavior of the downstream perturbed flow generally appears to have a poor correlation but looking closely at the data throughout the channel (Figure 10: $r = 0.6$, $\%_{\mathrm{Nrmse}} = 16\%$), there is noticeably less accurate match between the simulated results and physical experiments in the lower layer and in the close vicinity of the hub. However, the simulation does succeed in reproducing the vertical asymmetry of the TKE profile. This feature comes from the distinct nature of the top and bottom boundaries. The bottom boundary is a solid boundary characterized by a roughness height whereas the upper boundary is a fluctuating free-surface. The different natures of the top and bottom boundaries generate an asymmetrical velocity gradient throughout the depth, in spite of the vertical symmetry of the channel/turbine set-up, and therefore lead to a vertical asymmetry in the TKE profile. However, this vertical asymmetry appears to be amplified in the simulation especially in the lower boundary where TKE levels are under predicted. Potentially this could be due to the differences in the bottom boundary layer behavior alluded in the previous paragraph.

The origin of the asymmetry discrepancy between the simulated and experimental TKE profiles as well as the double maxima observed only in the simulations is not fully understood. It is however worth noticing that the Reynolds stress results from Myers and Bahaj (2010) (i.e. Figure 11) do replicate the double peaked structure with amplified vertical asymmetry behavior seen in the simulated TKE levels. This suggests that the simulations are properly reproducing the coherent stress generating turbulence arising from vortex shedding around the porous disk and that discrepancies arise from the small scale "grid" generated incoherent turbulence from the center of the porous disk. Thus it can be argued that the double peaked structure observed in the simulation is closer to true turbine behavior, the reproduction of which is the ultimate goal of the model development.
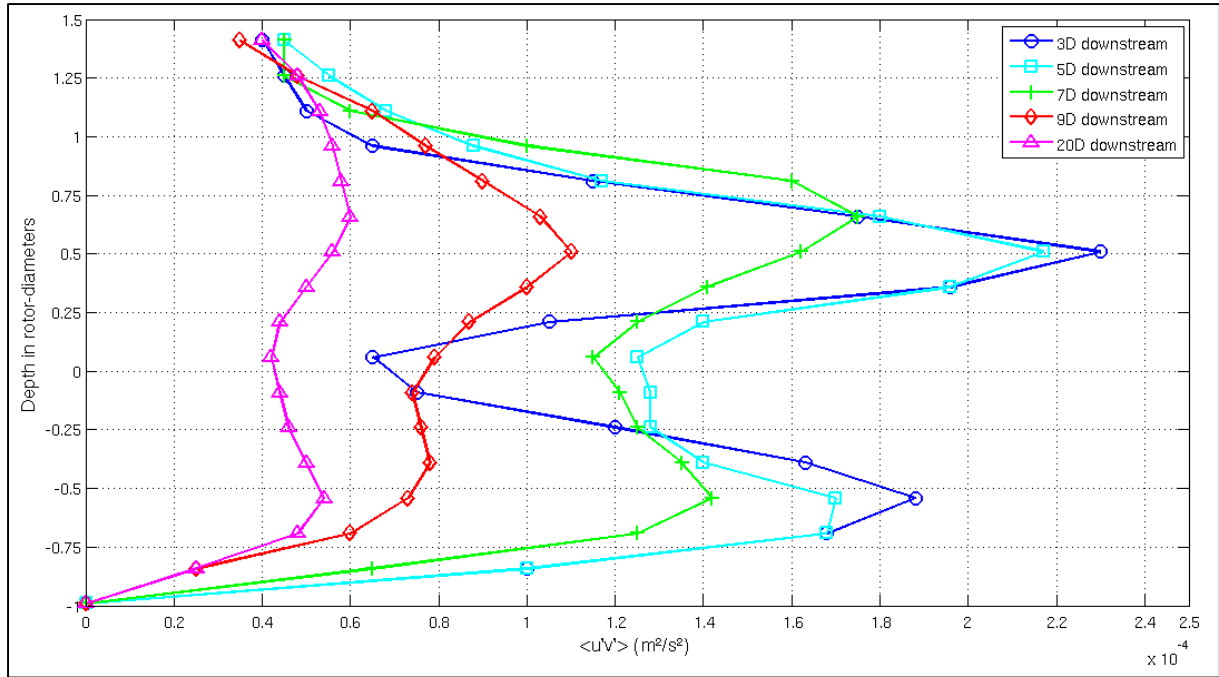
19

Figure 11: Vertical profiles of Reynolds stress at different locations downstream of the device – Experimental data from Myers and Bahaj, (2010).

Figure 12 displays comparison of the simulated and experimental horizontal transects of TKE taken on a mid-depth plane (Figure 2) at different locations downstream the device. The simulated TKE wakes are narrower than in the experiments, leading to a significant deviation ($\%_{\text{Nrmse}} =$ 39.7%) yet the correlation with the experiment is satisfactory ($r = 0.82$). The simulated peak magnitudes are lower than the experimental measurements, but this is likely to be because they are at the centre of the turbine and thus lie at the low point between the two peaks observed in Figure 12. The horizontal transects taken in Figure 12 are located right in the area where turbines and porous disks have fundamental difference in terms of "turbulence short-circuiting", and so a perfect match between experimental and simulated results cannot be expected.
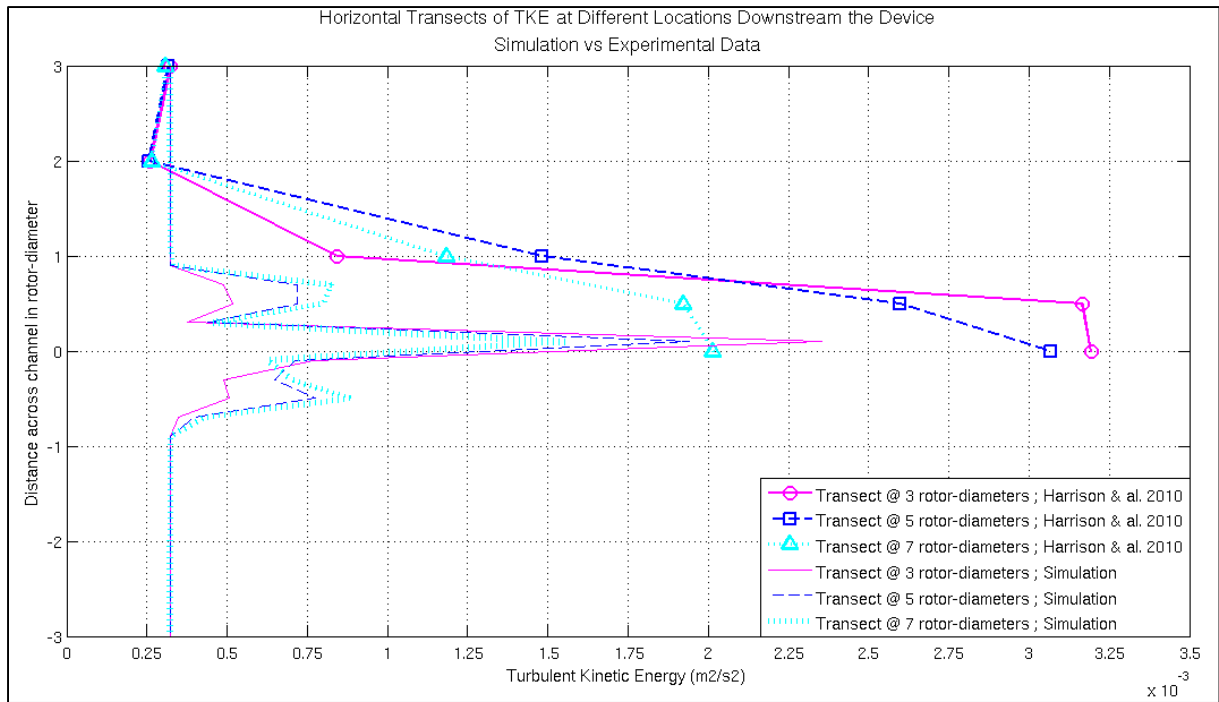
Figure 12: Horizontal transects of TKE at different locations downstream of the device – Experimental data versus simulated results. Experimental profiles (marked lines) are used as benchmarks to estimate the accuracy of their simulated equivalents (lines of matching colors and types).

Much if not all of the discrepancy in the lateral distribution of TKE is no doubt due to the implicit assumption in ROMS that TKE generation is derived from vertical shear whereas the axisymmetric nature of tidal turbines certainly suggests that lateral shear is equally important particularly on the mid-plane reproduced in Figure 12. This level of discrepancy in the lateral extent of turbulence production is probably an unavoidable consequence of the splitting between horizontal and vertical mixing present in ROMS. It is worth noting however that the lateral wake structure has been well represented in the simulations (Figure 8) and that the level of agreement observed in TKE prediction has to be put into perspective with the optimum level of confidence that can be expected for such a quantity (i.e. Appendix 1: Numerical Implementation).

5. Discussion

This paper describes a new method for representing TCT within an ocean circulation type model capable of performing regional scale simulations. The representation permits the TCT influence on the hydrodynamics to be modeled and this makes it suitable for TCT farm resource assessment as well as for assessment of environment impacts on the hydrodynamics. The new method is proven to be grid convergent, both spatially and temporally, and grid convergence tests have been used to identify the minimum grid spacing requirements. The new method is also demonstrated to reproduce the results of physical experiments with a single turbine in a channel to a good level of accuracy. The results do however highlight two features which must be considered in application of the model. The first is that, as with most circulation models, the results are relatively sensitive to the value of the eddy viscosity parameter and so appropriate data must be available to inform the selection of the value of this parameter. Secondly, the spatial resolution required to simulate the turbine effects discussed here will no doubt require either a nested grid and/or a

21

curvilinear mesh which provides local refinement to the region around an array, otherwise a high grid resolution applied in regions of lower requirement would lead to impractically high computational time and large grid size.

In addition, this paper highlights the importance of sub-grid scale turbulence in the TCT forcing parameterization especially regarding both momentum flow recovery and energy balance. Although empirical parameterization of the drag coefficient could result in simulated wake recovery similar to observation, it would misrepresent the energetic nature of the TCT perturbation and thus bias power yield assessments of any TCT array layout. In the same manner, the discrepancies noted in Figure 10 between simulated and experimental data as well as the mismatch of vertical shapes between the experimental profile from Figure 10 and the Reynolds stress profiles from Figure 11 suggest that the TCT-induced energy transfer may be misrepresented when the porous disc modeling approach is used. Furthermore, since porous discs convert energy that would be extracted from the flow by the rotating blades of a TCT into small-scale turbulence (Harrison, et al., 2009), one could presume that energy discrepancy between simulated and experimental data in Figure 10 is more representative of the energy captured by the device. Nevertheless, although in the vicinity of the device the axisymmetric nature of tidal turbines certainly suggests that lateral and vertical shears are equally important, ROMS considers that TKE generation is only derived from vertical shear. This limiting assumption needs to be kept in mind during resource assessments.

The method develop here has two advantages in comparison with an empirically-enhanced thrust-coefficient parameterization. Firstly it does not require fastidious empirical fitting of the thrust coefficient. Such an empirical approach would entail deriving a new data set for any change in flow or device features. Secondly, by realistically accounting for the turbulence influence in the flow perturbation, the present TCT representation method is able to provide an assessment of the meso-scale turbulence behavior induced by the device that is compulsory for TCT layout optimization, whereas an empirically enhanced thrust coefficient method would completely ignore this feature. We emphasize that the entire set of parameters (i.e. C_t, C_d, C_p, C_ψ) was assigned values following recommendations given in published literature (Réthoré, et al., 2009; Rados, et al., 2009; Myers & Bahaj, 2010) and that only one user adjustable parameter (i.e. the eddy viscosity) has been used in the simulations presented here. Whether this result will hold in general must be determined following tests with other TCT devices.

The numerical tool presented here is a unique platform that permits thorough optimization of TCT layout by simulating the entire hydrodynamics induced by the interaction between a TCT and its surrounding flow for scales ranging from the turbine blade to the estuary. In this respect, it appears as the first of its kind. Nevertheless, before applying this tool to real-world TCT array simulations, further validations need to be performed. Indeed, validations against in-situ measurements and/or experimental data of multi-device systems are necessary to assess the versatility of the model and its aptitude in simulating device interactions. It would also be interesting to investigate the accuracy of the free-surface perturbation related to the presence of TCTs that is predicted in this method, when suitable reference data becomes available. Additionally, further developments of numerical implementation are needed to make the tool more versatile. At this stage of numerical development, the TCT orientation coincides with the orientation of the grid and, the implementation implies that the device can work in both directions (ebb and/or flow) but cannot yaw. Additionally, testing the compatibility of the adapted ROMS code with its set of model extensions may to be conducted. For

example, ROMS can be coupled with codes accounting for wave forcing (SWAN), atmospheric forcing (WRF) or sediment transport (Website, n.d.), and thus open a boundless range of assessment options to the present TCT layout optimization tool.

6. Conclusions

To conclude, on the basis of comparisons with physical scale tests, a regional ocean modeling system (ROMS) has been successfully adapted to represent wake decay behind a marine current turbine in terms of both momentum and turbulence. Model alterations to achieve this required both the addition of momentum and turbulence source terms to the model in order to provide a full account of the hydrodynamic effects induced by an idealized stream turbine in the near and far fields. The model has been shown to be convergent and stable. Once the model has been properly set up and validated, model data comparisons utilizing the results of laboratory tests demonstrate the ability of the chosen implementation to adequately reproduce features of the turbine wake and its recovery.

Consequently, accounting for the TCT-induced turbulence phenomenon through GLS closure model corrections has been shown to be effective in compensating the sub-grid scale turbulence which is unresolved in ocean circulation models. It permits the use of computationally inexpensive techniques, such as the actuator disc theory, to simulate the wide range of TCT perturbation scales without losing the accuracy of both momentum and turbulence behaviors. Model weaknesses detected include a rather strong sensitivity to the eddy-viscosity calibration, the necessity of using nested or curvilinear meshing for realistic cases and the fact that, at the present stage of development, the grid geometry conditions the turbine orientation. As regards the requirements stipulated in the introduction, the present method is demonstrated to be a satisfactory approach for developing a TCT array optimization tool. In future work, the ability to simulate the interactions from multiple turbine wakes will be investigated and the simulation of full scale devices will be performed.

References

Bai, L., Spence, R. R. G. & Dudziak, G., 2009. *Investigation of the Influence of Array Arrangement and Spacing on Tidal Energy Converter (TEC) Performance using a 3-Dimensional CFD Model.* Uppsala, s.n.

Blunden, L. S. & Bahaj, A. S., 2007. Tidal Energy Resource Assessent for Tidal Stream Generators. *Proceedings of the Institution of Mechanical Engineers,* Volume 221(A2), pp. 137-146.

Bryden, I. G. & Couch, S. J., 2004. *ME1 - Marine Energy Extraction: Tidal Resource Analysis.* Denver, Renwable Energy, pp. 133-139.

Bryden, I. G. & Couch, S. J., 2007. How Much Energy Can Be Extracted from Moving Water with a Free Surface: A Question of Importance in the Fiel of Tidal Current Energy ?. *Renewable Energy,* Volume 32(11), pp. 1961-1966.

Bryden, I. G. & Melville, G., 2004. Choosing and Evaluating Sites for Tidal Current Development. *Journal of Power and Energy,* Volume 218, pp. 567-577.

Buhl, M. L., 2005. *A New EMpirical Relationship between Thrust Coefficient and Induction Factor for the Turbulent Windmill State,* s.l.: s.n.

Burton, T., Sharpe, D., Jenkins, N. & Bossayi, E., 2008. *Wind Energy Handbook.* s.l.:John Wiley & Sons Ltd.

Canuto, V. M., Howard, A., Cheng, Y. & Dubivikov, M. S., 2001. Ocean turbulence I: one-point closure model. Momentum and heat vertical diffusivities. *Jouranl of Physical Oceanography,* Volume 31, pp. 1413-1426.

Carter, G. S. & Merrifield, M. A., 2007. Open Boundary Conditions for Regional Tidal Simulations. *Ocena Modelling,* Volume 18, pp. 194-209.

Chen & Kim, 1987. *Computation for turbulent flow using an extended closure model,* s.l.: s.n.

Couch, S. J. & Bryden, I. G., 2006. Tidal Current Energy Extraction: Hydrodynamic Resource Characteristics. *Proc. IMechE,* Volume 220, pp. 185-194.

Daly, T., Myers, L. E. & Bahaj , A. S., 2010. *Experimental analysis of the local flow effects around single row tidal turbine arrays.* Bilbao, s.n.

Draper, S., Houlsby, G. T., Oldfield, M. L. G. & Borthwick, A. G. L., 2009. *Modelling Tidal Energy Extraction in a Depth-Averaged Coastal Domain.* s.l., s.n.

Garrett, C. & Cummins, P., 2005. The power potential of tidal currents in channels. *Proc. of the Royal Society A-Mathematical Physical and Engineering Sciences,* Volume 461(2060), pp. 2563-2572.

Gretton, G. I., Bruce, T. & Ingram, D. M., 2009. *Hydrodynamic modelling of a vertical axis tidal current turbine using CFD.* Uppsala, s.n.

Haidvogel, D. B. & Beckmann, A., 1999. *Numerical Ocean Circulation Modeling.* s.l.:Imperial College Press.

Harrison, M. E., Batten, W. M. J., Myers, L. E. & Bahaj, A. S., 2009. *A Comparison between CFD SImulations and Experiments for Predicting the far Wake of Horizontal Axis Turbines.* Uppsala, s.n.

Kantha, L. H. & Clayson, C. A., 1994. Numerical Models of Oceans and Oceanic Processes.. In: *International Geophysics Series.* San Diego: Academic Press, p. 940.

Karsten, R. H., McMillan, J. M., Lickley, M. J. & Haynes, R. D., 2008. Assessment of tidal current energy in the Minas Passage,Bay of Fundy. *Journal of Power and Energy,* Volume 222, pp. 493-507.

Kasmi, E. & Masson, C., 2008. An extend k-ε model for turbulent flow through horizontal-axis wind turbines. *J. of Wind Eng. & Ind. Aero.,* Volume 96, pp. 103-122.

Kawase, M. & Thyng, K. M., 2009. *A Three-dimensional Hydrodynamic Model of Inland Marine Waters of Washington State, United States, for Tidal Resource and Environmental Impact Assessment.* Uppsala, s.n.

Kolmogorov, A. N., 1941. On degeneration of isotropic turbulence in an incompressible viscous liquid. *Comptes Rendus (Doklady) de l'Academie des Sciences de l'U.R.S.S.,* Volume 31, p. 538–540.

Lalander, E. & Leijon, M., 2009. *Numerical modeling of a river site for in-stream energy converters.* Uppsala, s.n.

Maganga, F. et al., 2009. *Experimental Study to Determine Flow Characteristic Effects on Marine Current Turbine Behaviour.* Uppsala, s.n.

Myers, L. E. & Bahaj, A. S., 2010. Experimental analysis of the flow field around horizontal axis tidal turbines by use of scale mesh disk rotor simulators. *Ocean Engineering,* Volume 37, pp. 218-27.

O'Doherty, T. et al., 2009. *Experimental and Computational Analysis of a Model Horizontal Axis Tidal Turbine.* Uppsala, s.n.

Pham, C.-T. & Martin, V. A., 2009. *Tidal current turbine demonstration farm in Paimpol-Bréhat (Brittany): tidal characterisation and energy yield evaluation with Telemac.* Uppsala, s.n.

Rados, K. G. et al., 2009. *CFD modeling issues of wind turbine wakes under stable atmospheric conditions.* s.l., s.n.

Réthoré, P.-E. & Sorensen, N. N., 2008. *Actuator disc model using a modified Rhie-Chow/SIMPLE pressure correction algorithm.* Brussels, s.n.

Réthoré, P.-E., Sørensen, N. N., Bechmann, A. & Zhale, F., 2009. *Study of atmospheric wake turbulence of a CFD actuator disc model.* Marseille, s.n.

Roc, T., Conley, D. C. & Greaves, D., 2010. *Accounting for Turbulence in a Regional Numerical Model for Tidal Current Farm Planning.* Bilbao, s.n.

Roc, T., Conley, D. C. & Greaves, D., 2011. *Turbulence Correction Terms for Representing Tidal Current Turbines in a Regional Ocean Model for Array Planning and Impact Assessment.* Maui, s.n.

Salter, S. H., 2009. *Correcting the Under-estimate of the Tidal-Stream Resource of the Pentland Firth.* Uppsala, s.n.

Sanz, C., 2003. A note on k-ε modeling of vegetation canopy air-flows. *Boundary-Layer Meteorology,* Volume 108, pp. 191-197.

Shcheptkin, A. F. & Mc Williams, J. C., 2005. The Regional Oceanic system (ROMS): a split-explicit, free-surface, topography-following-coordinate oceanic model. *Ocean Modelling,* Volume 9, pp. 347-404.

Sorensen, J. N. & Shen, W. Z., 2002. Numerical Modeling of Wind Turbine Wakes. *J. of Fluids Engineering,* 124(2), pp. 393-399.

Sun, X., Chick, J. P. & Bryden, I. G., 2008. Laboratory-scale simulation of energy extraction from tidal currents. *Renewable Energy,* Volume 33, p. 1267–1274.

Sutherland, G., Foreman, M. & Garrett, C., 2007. Tidal current energy assessment for Johnstone Strait, Vancouver Island. *Journal of Power and Enery,* 221(A2), pp. 147-157.

Umlauf, L. & Burchard, H., 2001. A generic length-scale equation for geophysical turbulence models. *Journal of Marine Research,* Volume 61(2), pp. 235-265.

Umlauf, L. & Burchard, H., 2005. Second-order turbulence closure models for geophysical boundary layers. A review of recent work. *Continental Shelf Research,* 25(7-8), pp. 795-827.

Umlauf, L., Burchard & Hutter, K., 2003. Extending the k-ω turbulence model towards oceanic applications. *Ocean Modelling,* Volume 5, pp. 195-218.

Website, n.d. *Regional Ocean Modeling System (ROMS).* [Online] Available at: http://www.myroms.org

Whelan, J., Thomson, M., Graham, J. M. R. & Peiro, J., 2007. *Modelling of free surface proximity and wave induced velocities around an horizontal axis tidal stream turbine.* Porto, s.n.

Appendix 1: Numerical Implementation

In order to implement these physical terms into ROMS, several mathematical and numerical adaptations had to be performed. To illustrate these adaptations, consider the case of an orthonormal grid in which the device is defined over a unique grid cell-volume (Figure 13).
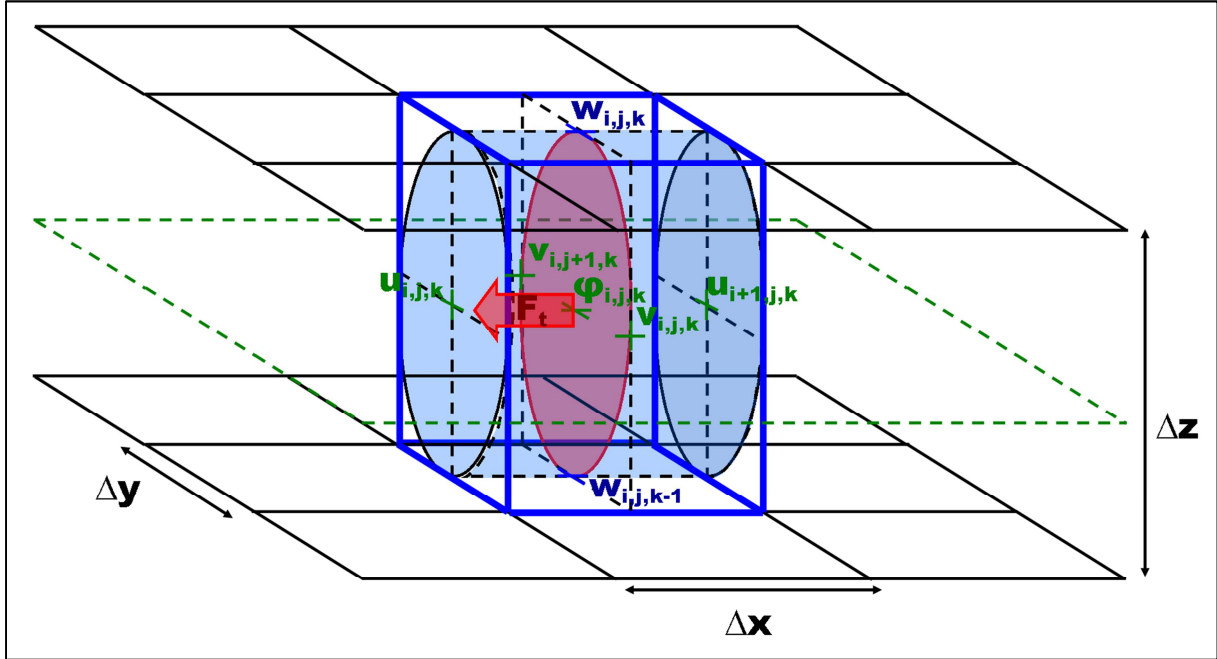

Figure 13: Staggered Grid & Control Volume. The diagram displays staggered horizontal grids at the z_w (*N, N+1*) levels (black lines), the z_ρ (*N*) level (green dashed plane), the actuator disc (red surface), the "smeared" actuator cylinder (light blue volume), the numerical control volume (heavy blue solid lines) and its median

planes (dashed black lines). It also displays spatial distribution on ROMS 3-D staggered grid of the velocity components (u,v,w) and the turbulence point (φ).

On such a staggered grid, the components of the flow-velocity (*u,v,w*) and the turbulent quantities (TKE, TLS) are computed at different locations; the latter being located at the *φ*-points. For the sake of generalization and further development, the center of the "real" rotor disc is positioned on a *φ*-point (i.e. red disc on Figure 13) and thus surrounded by the flow-velocity points. However in ROMS' code, the body-force $\overrightarrow{F_t}$ can only be defined on the *u/v* points and more precisely here on the *u* points since $\overrightarrow{F_t}$ is aligned with the incoming flow-velocity vector in this case. In other terms, the staggered grid implies that the thrust force is transformed into pressure jumps at each surrounding cell face, namely at the upstream and downstream *u*-points. Equation (24) ensures the equivalence between the pressure discontinuities and the related force density present in the control volume.

$$\iiint_V \overrightarrow{F'}\, dV = \iint_S pdS\vec{n} \tag{24}$$

A simplified Rhie-Chow numerical scheme (Réthoré & Sorensen, 2008) is used to calculate the distribution of the force over the neighboring cells.

$$\overrightarrow{F'_{i,J,k}}V_{i,j,k} = \frac{1}{2}\sum_{j}^{j+1} p_{i,j,k}S_{i,j,k}\,\overrightarrow{n_{i,J,k}} \tag{25}$$

Here, $\overrightarrow{F'_{i,J,k}}$ symbolizes the force density ($N.m^{-3}$), $V_{i,j,k}$ the volume of the control volume (m^3) (i.e. $V_{i,j,k} = \Delta x \times \Delta y \times \Delta z$)), $\overrightarrow{n_{i,J,k}}$ the normal vector to the cell face, $S_{i,j,k}$ the vertical cell surface (m^2) and $p_{i,j,k}$ the dynamic pressure at the vertical cell surface ($N.m^{-2}$). The pressure jump, p, corresponds to the dynamic pressure exerted by a moving fluid of velocity $\vec{v}$ on a blocking surface and can be expressed as follows:

$$p = -\frac{1}{2}\rho C|\vec{v}|\vec{v}.\vec{n} \tag{26}$$

where C is the drag coefficient derived from Eq. (18), given by,

$$C = 4 \times \frac{1 - \sqrt{1 - C_t}}{1 + \sqrt{1 - C_t}} \tag{27}$$

Equation (25) gives the following final split expression:

$$\overrightarrow{F'_{i,J,k}}V_{i,j,k} = \begin{cases} -\frac{1}{4}\rho C S_{i,j,k}\left(\sum_{j}^{j+1} u_{i,j,k}|u_{i,j,k}|\right)\overrightarrow{n_{i,J,k}}\,;\ at\ the\ upstream\ U\ point \\[4mm] -\frac{1}{4}\rho C S_{i,j,k}\left(\sum_{j-1}^{j} u_{i,j,k}|u_{i,j,k}|\right)\overrightarrow{n_{i,J,k}}\,;\ at\ the\ downstream\ U\ point \end{cases} \tag{28}$$

This implementation has an additional advantage. By splitting the pressure discontinuity generated by the presence of the device into two pressure jump contributions at the two cells adjacent faces, numerical "pressure wiggles" (Réthoré & Sorensen, 2008) may be avoided. However, $\overrightarrow{F'}$ is not the same as the original thrust force $\overrightarrow{F_t}$.

27

Although they are both body-forces, $\overrightarrow{F'}$ results from the integration of the numerical force density over the control volume V whereas $\overrightarrow{F_t}$ results from the integration of the drag and lift forces over the volume swept by the turbine's blades (Sorensen & Shen, 2002). This volume of integration correspond to the actuator disc surface multiplied by the apparent width of the turbine blades, W. The apparent width can be expressed in function of the blade chord length, L_{chord}, and the blade pitch angle, θ as follows

$$W = L_{chord}\, sin\,\theta \tag{29}$$

Consequently, in order to be consistent with the original thrust force, irrespectively of the width of the numerical control-volume Δx, $\overrightarrow{F'}$ must verify the following equation:

$$\overrightarrow{F_t}\left(\frac{\pi D^2}{4}W\right) = \overrightarrow{F'}\left(\frac{\pi D^2}{4}\Delta x\right) \tag{30}$$

In equation (30), D is the rotor diameter (m). In this manner and by introducing the drag coefficient from Eq. (18), the equivalence between the original thrust force and the smeared numerical force is respected:

$$\overrightarrow{F'_{i,j,k}}V_{i,j,k} = \begin{cases} -\dfrac{L_{chord}\, sin\,\theta}{4\Delta x}\displaystyle\sum_{j}^{j+1} \overrightarrow{n_{i,j,k}}\, S_{i,j,k}\rho C u_{i,j,k}\left|u_{i,j,k}\right| \;;\; at\ the\ upstream\ U\ point \\[4mm] -\dfrac{L_{chord}\, sin\,\theta}{4\Delta x}\displaystyle\sum_{j-1}^{j} \overrightarrow{n_{i,j,k}}\, S_{i,j,k}\rho C u_{i,j,k}\left|u_{i,j,k}\right| \;;\; at\ the\ downstream\ U\ point \end{cases} \tag{31}$$

The turbulence correction terms (Eq. (19) and (20)), and the set of parameters (C_p, C_d, C_ψ) require calibration based on analytical analysis of the validation tests described in Section 4.2 and those previously carried out (Sanz, 2003; Réthoré, et al., 2009; Kasmi & Masson, 2008; Rados, et al., 2009; Chen & Kim, 1987). Additionally, because of the volumetric implementation method required by the ROMS grid structure, C_d, C_p and C_ψ are weighted according to the control volume dimensions as is the case for $\overrightarrow{F'}$. Here, (C_p, C_d, C_ψ) are found to be equivalent to Eq. (32).

$$\begin{cases} C_p = C_1\left(C_{pw}\dfrac{L_{chord}\, sin\,\theta}{\Delta x}\right) \\[3mm] C_d = C_2\left(C_{pw}\dfrac{L_{chord}\, sin\,\theta}{\Delta x}\right) \\[3mm] C_\psi = C_3\left(C_{pw}\dfrac{L_{chord}\, sin\,\theta}{\Delta x}\right)^2 \end{cases} \tag{32}$$

The coefficients C_1, C_2 and C_3 are given by Réthoré (2009) and Rados *et al.* (2009). Their relationship with $\left(C_{pw}\dfrac{L_{chord}\, sin\,\theta}{\Delta x}\right)$ and the magnitude of C_{pw} result from an empirical approach based on the different validation tests performed during the development of the present method. Issuing from this development phase, C_{pw} has been found to be a function of the design feature C_t as suggested by Réthoré (2009).

$$C_{pw} = C_t\sqrt{1 - C_t} \tag{33}$$

Interestingly and in accordance with the definition of the induction factor and Eq. (6), a parallel can be drawn between C_{power} and C_{pw} since:

$$C_{power} = C_t \frac{U_d}{U_\infty} \; ; \; C_{pw} = C_t \frac{U_w}{U_\infty} \tag{34}$$

Regarding the integration of the turbulence correction terms (Eq. (20)) on the ROMS grid, the turbulence quantities are computed at the φ-points (Figure 13). Consequently, the volume where the correction terms are injected is bounded by the neighboring cells faces. As a result of this compulsory volume smearing, the issue raised by Sanz (2002) of delimiting the volume of application of the turbulence balance correction is avoided. The implementation scheme of the three turbulence correction terms (Eq. (19)) can then be expressed as:

$$\begin{cases} P_{k\,i,j,k} = C_p \dfrac{\left(\frac{1}{2}\left|u_{i+1,j,k} + u_{i,j,k}\right|\right)^3}{\Delta x} - C_d \dfrac{\frac{1}{2}\left|u_{i+1,j,k} + u_{i,j,k}\right| k_{i,j,k}}{\Delta x} = P_{p\,i,j,k} - P_{d\,i,j,k} \\[4mm] P_{\psi\,i,j,k} = C_\psi \dfrac{P_{i,j,k}^2}{\varepsilon_{i,j,k}} \; ; \end{cases} \tag{35}$$

where $P_{i,j,k}$ represents the turbulence production by vertical shear (Umlauf, et al., 2003) and C_p, C_d and C_ψ come from Equation (32). It is worth noting that the weight applied on P_ψ (i.e. $C_\psi C_v{}^2$) has been empirically validated during the validation and grid-dependency test series which will be presented in the next chapters. The set of $\left(\overrightarrow{F'_{i,j,k}}, P_{p\,i,j,k}, P_{d\,i,j,k}, P_{\psi\,i,j,k}\right)$ constitutes the core of the TCT modeling adaptation implemented in ROMS.

In practice, defining the volume control $V_{i,j,k}$ as a one cell-cube is too coarse and would generate information loss. Representation of the "rotor cylinder" in the structured grid of ROMS, as shown in Figure 14, is dependent of the grid resolution and will never perfectly match the cylindrical volume. However, after a certain numerical resolution threshold, the resulting discrepancies between finer resolutions induced by the volume approximation can be neglected as demonstrated in Section 4.1.
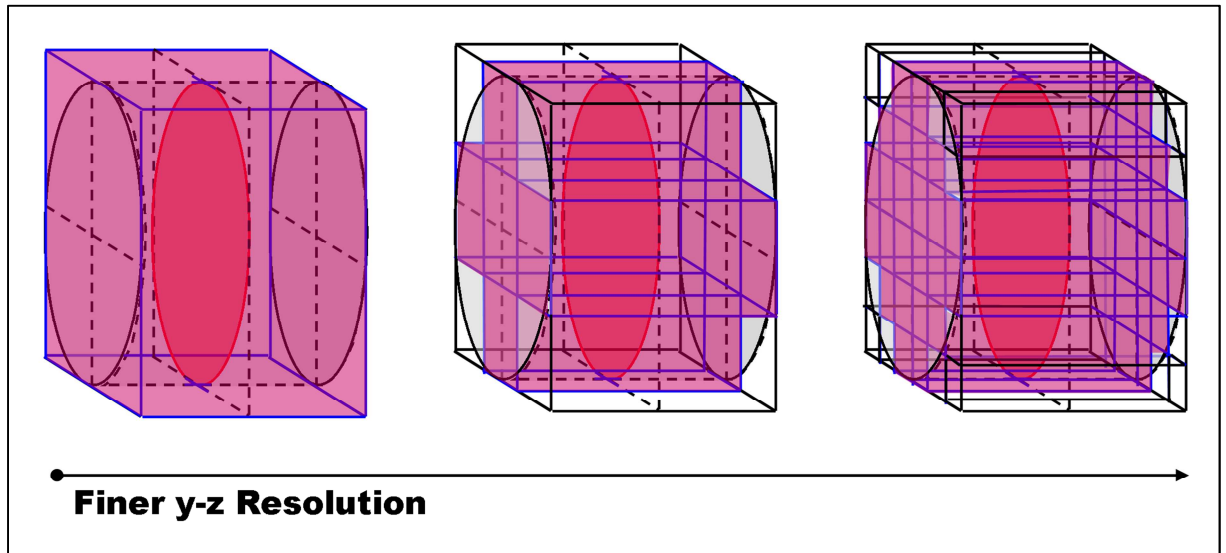

Finer y-z Resolution

Figure 14: Comparison between numerical control-volume approximations (red volumes) for finer and finer y-z resolutions (left to right) with the exact "smeared" control volume (blue cylinder). The red disc represents the actuator disc.